Journal of Materials and Manufacturing 5(2): 119-148 (2026)

JMM Materials and Manufacturing Journal of Materials and Manufacturing

Divergence of the Initial and Peak Secant Stiffness in the Low-Velocity Impact Response of Curved Woven T300/914 Panels and Energy-Equivalent Delamination Area

Onur Gök[a,*], H. Hüseyin Taşer[a], Lokman Gemi[a,b]

[a]*Konya Organized Industrial Zone Vocational School, Necmettin Erbakan University, 42000 Konya, Türkiye*
[b]*Faculty of Engineering and Architecture, Department of Mechanical Engineering, Recep Tayyip Erdoğan University, Rize, Türkiye*
(ORCID: 0000-0003-1160-1963), ogok@erbakan.edu.tr
(ORCID: 0000-0001-5138-9085), hhtaser@erbakan.edu.tr
(ORCID: 0000-0002-9895-6574*), lgemi@erbakan.edu.tr*

Abstract

The low-velocity impact response of woven T300/914 carbon/epoxy cylindrical shell panels was examined numerically at six curvature levels extending from the flat plate to the half cylinder, with a constant projected span of 125 mm and a thickness of 1 mm, using SC8R continuum shell models carrying Hashin intralaminar damage and three cohesive interfaces, at an energy of 6.70 J. Curvature raised the initial tangent stiffness by 74 per cent while it lowered the peak force by 18 to 23 per cent and extended the contact duration from 17.2 ms to 20.0 to 21.9 ms. The initial stiffness predicts these two trends in the opposite direction. The divergence between the initial and peak stiffnesses begins before damage, and the ratio of the secant stiffness at first damage to the initial stiffness is 1.33 in the flat plate and 0.60 in the half cylinder. The hoop stresses taken along the arc are consistent with this divergence. While the flat plate carries an average tension of 141 MPa on the outer arc at the peak force, this value remains between 2.5 and 31 MPa in the curved panels, and the hoop compression near the contact turns into tension around first damage. In this series, in which the impactor mass is 232 to 367 times the panel mass, the contact duration is consistent with the expression $\pi\sqrt{(m/K_{sec})}$ within 8.9 per cent. Since K_{sec} is read from the response itself, this relation is reported as consistency, not as prediction. The relation $D/G_c = d/(r - (r - 1)d)$ between the damage variable and the dissipated energy was derived from the bilinear cohesive law. For the card used, r = 112.6, and 0.9 per cent of the fracture energy is dissipated at the 0.5 level of d. For a mode-dependent card, r remains between 207 and 327. The energy-equivalent area defined with this relation is between 122 and 262 mm². The area of the 0.5 threshold is 3 to 12 times this, and the fully separated area is 1.6 to 4.5 times below it. The results belong to a numerical framework without experimental validation, solved with a single mesh, a single impact energy and a single impactor mass.

Keywords: Low-velocity impact, woven carbon/epoxy, shell curvature, secant stiffness, cohesive zone model

1. Introduction

Low-velocity impact damage in fibre-reinforced laminates develops through three mechanisms acting together. Intralaminar matrix cracking and fibre rupture, interlaminar delamination and back-face fibre fracture progress within the same event. In a thin laminate, which of these mechanisms governs the load-carrying capacity depends on the geometry of the panel. Early experimental studies on the woven T300/914 system documented the characterisation of indentation damage [1], the fatigue life of the impact-damaged laminate [2] and the development of damage in three-point beam impact [3]. On the numerical side, Tita and co-workers showed that a shell model without cohesive interfaces cannot represent delamination in thin laminates and departs from the experiment in some regions of the force against displacement curve [4]. The addition of

* Corresponding author
E-mail addresses: ogok@erbakan.edu.tr
DOI: 10.5281/zenodo.23662240
Received: 18 September 2026, Revised: 20 October 2026, Accepted: 26 October 2026
ISSN: 2822-6054 ©2026 The Author(s). Published by JMM under CC BY 4.0

cohesive interfaces closed this gap, and Feng and Aymerich predicted both the initiation and the propagation of damage in agreement with the experiment [5]. Approaches based on continuum damage mechanics [6] and multiscale formulations based on the micromechanics of failure [7] are different branches of the same framework. A systematic comparison of combinations of damage criterion, evolution law and interface model showed that the impact response is determined by the evolution law and the delamination by the interface model [8]. The same modelling framework has been used for fibre orientation [9], thermoplastic, short-fibre and non-crimp fabric reinforced systems [10, 11, 12], the strain field around the damage [13] and the compression after impact strength [14], and the effects of thickness, stitch density and edge impact in stitched laminates have been studied separately [15, 16, 17].

In impact models solved with cohesive interfaces, the delamination area is reported as the area of the region in which the interface damage variable exceeds a certain threshold. The threshold is generally taken as zero or 0.5, a value of 0.8 has also been used in woven shells [18], and the reason for the choice is mostly not given. The damage variable, however, is by definition a ratio of stiffness loss and is not equal to the ratio of dissipated energy. In the bilinear traction separation law the relation between these two ratios can be written in closed form, and it is a strongly nonlinear relation that depends on the stiffness, strength and fracture energy values of the card. The consequence is that areas reported with two different thresholds differ from each other by an order of magnitude and that neither of them represents the energy dissipated at the interface. In this study this relation was derived and the energy-equivalent area defined with it was compared with the threshold areas.

Weave architecture and laminate thickness are two geometric variables that govern the impact response, and the literature built on these two variables has produced a consistent expectation. Belingardi and Vadori measured that both the first damage force and the peak force rise linearly as the number of plies increases [19]. The same trend has been reported in thick woven laminates [20], in woven structures for automotive applications [21] and for the stacking effect in braided panels [22]. Modelling studies validated on different stacking sequences [23], the in-plane compression response after impact [24], the comparison of two different progressive damage models in a woven composite [25], the effect of the weave pattern [26] and the multiscale damage analysis of three-dimensional woven composites [27] extend this framework. It has been reported that in oblique impact the damage initiation force and time rise together as the z-direction fibre volume fraction increases [28], and that in repeated impact the contact duration and the peak force increase together, which is regarded as an indicator of the change in the local laminate stiffness [29]. The common result of these studies is that the peak force increases as the stiffness increases.

It is known that curved shell geometries change the impact response. In studies on curved shells, however, curvature has either been held constant or scanned only in unidirectional laminates. Zhao and co-workers examined the quasi-static indentation, low-velocity impact and resonance responses of a doubly curved laminated panel under various boundary conditions and scanned variables such as the number of plies and the modulus ratio while holding the curvature ratio constant [30]. Ferreira and co-workers examined, in comparison with experiment, the effect of the cohesive stiffness and strength on the force history and on the delamination prediction in semi-cylindrical woven glass shells [18]. In filament-wound GFRP pipes, damage development and the role of delamination were documented with the ring tensile test [31], and in tubes the combined effect of winding angle and number of plies on the impact behaviour was addressed by experiment together with a Hashin-based cohesive model [32]. In the analytical solution derived for three-dimensional woven plates it was reported that the contact duration increases only with the impact velocity and depends very little on the impactor mass [33]. Olsson established through a mass criterion that, when the ratio of the impactor mass to the panel mass is large, the response is quasi-static rather than wave controlled and can be described by a single degree of freedom mass spring model [34]. In the previous studies of the first author, the curvature height was scanned for unidirectional T300/5208 laminates and a maximum of the peak force was found at intermediate curvature [35], and the effect of the stacking architecture was addressed first with an intralaminar-only damage model [36] and then, in a framework with nine cohesive interfaces, through lamination parameters and orientation entropy [37]. Since these studies did not separate the initial stiffness from the effective stiffness at the peak, the mechanism by which curvature changes the peak force could not be determined in woven shells.

This study examines why curvature lowers the peak impact force of a thin woven shell while it raises its initial stiffness, and to which physical quantity the delamination area reported from a cohesive model

corresponds. Six curvature levels were solved under a constant projected span and a constant thickness, with intralaminar and interlaminar damage modelled together. Since the impactor mass is more than two hundred times the panel mass, the response is in the quasi-static regime, and the mass spring relations of this regime were tested in the six panels. The initial tangent stiffness, the secant stiffness at first damage and the secant stiffness at the peak were measured separately, and the pre-damage hardening and softening were followed through the hoop stresses taken along the arc. Since the secant stiffness at the peak is read from the response itself, it was used not as a predictive tool but as a consistency measure of the quasi-static description. The closed-form relation between the cohesive damage variable and the dissipated energy was derived, the energy-equivalent delamination area was defined, computed from the exported damage fields and compared with the threshold areas. Since the resin, the cure and the weave architecture are held constant throughout the series, the only variable is geometry. The study contains no experimental validation, all models were solved with a single mesh, a single impact energy and a single impactor mass, and there is a residual in the solver energy balance that grows with curvature. To what extent the residual and the dependence of the area measures on resolution can affect the results was tested from the existing outputs, and the limits are collected in Section 5.4.

2. Model and method

2.1. Geometry and curvature series

The six panels were obtained by changing the sagitta of a cylindrical shell. The horizontal projected span in the curved direction of 125 mm, the panel width of 75 mm and the laminate thickness of 1 mm are constant in all configurations. The sagitta f was increased from zero to 62.5 mm in six equal steps, and a series extending from the flat plate to the half cylinder was built (Figure 1). The normalised sagitta f/a, defined with the half span a = 62.5 mm, advances from zero to one in steps of 0.2. In the finite element models the inner-surface radius was held fixed and the thickness was added outwards, so that the apex of the outer surface stays in the same plane in all panels and the impactor position does not change. The radius given in Table 1 is the inner-surface radius by this definition.

When the projection is held constant, the arc length and therefore the panel area and mass increase with curvature. The panel mass is 15.000 g in the flat plate and 23.749 g in the half cylinder. Since the impactor mass is 5.5 kg, the ratio of the impactor mass to the panel mass stays between 367 and 232 along the series. The response regime is determined from this ratio in Section 3.2. In the half cylinder the arc angle reaches 90 degrees and the support edge becomes parallel to the loading direction, and a6 has therefore been followed as a limiting case along the series.

Table 1. Panel geometry of the six curvature levels. R_{in} is the inner-surface radius, which is held fixed in the finite element models, θ_{max} the half opening angle, s the arc length along the curved direction, m_p the mass of the full panel and m/m_p the impactor-to-panel mass ratio.

Panel	f (mm)	R_{in} (mm)	θ_{max} (deg)	s (mm)	f/a (-)	m_p (g)	m/m_p (-)
a1	0.0	flat	0.00	125.00	0.0	15.000	367
a2	12.5	162.500	22.62	128.70	0.2	15.444	356
a3	25.0	90.625	43.60	138.68	0.4	16.643	330
a4	37.5	70.833	61.93	154.19	0.6	18.503	297
a5	50.0	64.062	77.32	174.24	0.8	20.909	263
a6	62.5	62.500	90.00	197.92	1.0	23.749	232

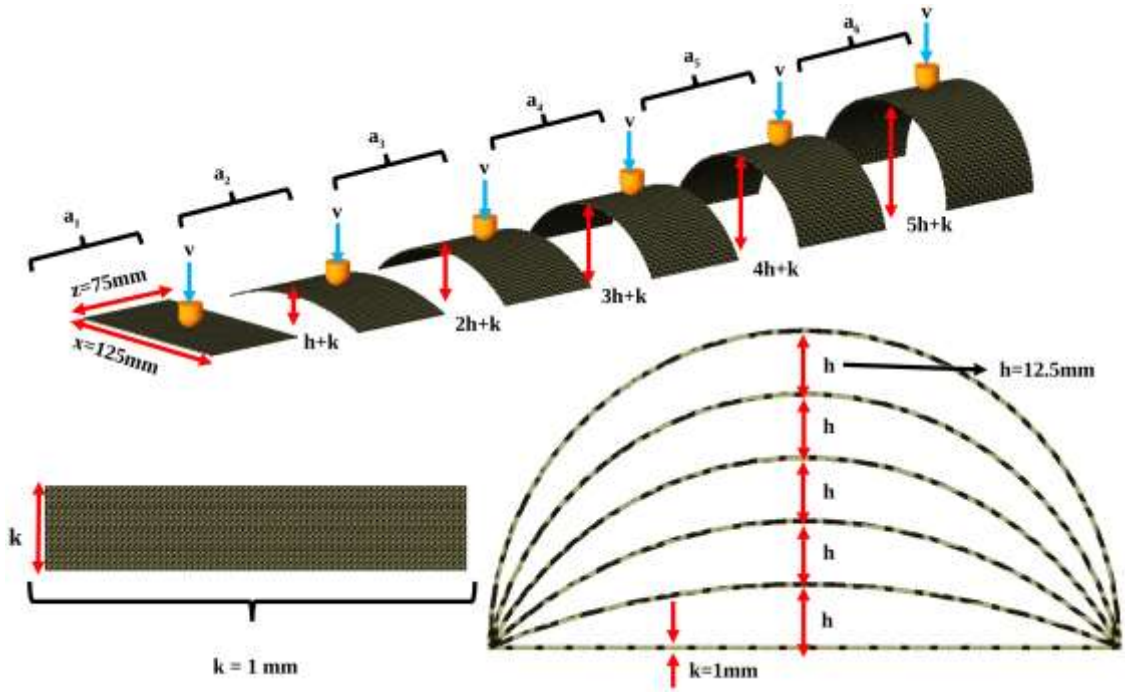

Fig. 1. Curvature series and panel geometry. The sagitta increases from a1 (flat) to a6 (half cylinder) while the projected span x = 125 mm, the width z = 75 mm and the laminate thickness k = 1 mm are held constant. The impactor position, marked by the arrow, is identical in every configuration.

2.2. Geometry and curvature series

The balanced woven T300/914 carbon/epoxy system was used. The elastic constants and the strengths were taken from measurements made on the same material system at three strain rates [38]. Owing to the weave architecture, the modulus and the strength in the two in-plane directions are equal. Intralaminar damage is initiated by four independent Hashin criteria,

$$F_i = f_i(\sigma_{11}, \sigma_{22}, \tau_{12}; X_T, X_C, Y_T, Y_C, S_L, S_T) \geq 1, \qquad i = 1 \ldots 4 \tag{1}$$

and the corresponding damage variable is advanced from zero to one by linear softening based on the fracture energy,

$$d_i = \frac{\delta_i^f(\delta_i - \delta_i^0)}{\delta_i\left(\delta_i^f - \delta_i^0\right)}, \qquad G_i = 1/2\ \sigma_i^0\ \delta_i^f \tag{2}$$

Here δ_i is the equivalent displacement, δ_i^0 its value at damage initiation and δ_i^f its value at complete damage. A fracture energy of 2.0 N/mm was taken for all four modes, and viscous regularisation at the level of 1×10^{-5} was applied for numerical stability. In the balanced weave the directions 1 and 2 represent the two fibre families, for which reason the name matrix tension from unidirectional lamina terminology was not used here, and the corresponding mode is referred to as the 2-direction tension mode. The card of the model defined by Equations 1 and 2 is collected in Table 2.

Table 2. Woven T300/914 lamina card. The elastic constants and the strengths are the values measured on the same material system and reported in [38]. The laminate stiffnesses follow from classical lamination theory for the stacking given in the table.

Group	Property	Symbol	Value	Unit
Woven lamina	Longitudinal modulus	E_1	69000	MPa
	Transverse modulus	E_2	69000	MPa
	In-plane Poisson ratio	ν_{12}	0.04	-
	Shear moduli	$G_{12} = G_{13} = G_{23}$	7100	MPa
	Density	ρ	1.6×10^{-9}	ton mm^{-3}
Hashin strengths	Longitudinal tensile	X_T	640	MPa
	Longitudinal compressive	X_C	540	MPa
	Transverse tensile	Y_T	640	MPa
	Transverse compressive	Y_C	540	MPa
	Longitudinal shear	S_L	180	MPa
	Transverse shear	S_T	180	MPa
Damage evolution	Fracture energy, all four modes	G	2.0	N mm^{-1}
	Viscous regularisation	η_d	1×10^{-5}	-
Laminate	Sublaminate thickness	t_s	0.25	mm
	Total thickness	t	1.00	mm
	Stacking	$[0]_4$ woven	3 cohesive interfaces	-
	In-plane stiffness	A_{11}	69110.58	N mm^{-1}
	Bending stiffness	D_{11}	5759.21	N mm
	Coupling matrix	B_{ij}	0	-

The one-millimetre laminate was divided into four sublaminates, each 0.25 mm thick, and three cohesive interfaces were placed between them. The interface was represented by surface-based cohesive behaviour. Damage initiation is given by the quadratic traction criterion,

$$\left(\frac{\langle t_n \rangle}{t_n^0}\right)^2 + \left(\frac{t_s}{t_s^0}\right)^2 + \left(\frac{t_t}{t_t^0}\right)^2 = 1 \tag{3}$$

and propagation follows the Benzeggagh-Kenane mixed-mode law,

$$G_c = G_{Ic} + (G_{IIc} - G_{Ic}) \left(\frac{G_{II}+G_{III}}{G_I+G_{II}+G_{III}}\right)^{\eta_{BK}} \tag{4}$$

In Equations 3 and 4 the penalty stiffness $K = 1 \times 10^6$ N/mm³, the nominal strength $t^0 = 73$ MPa and the fracture energy of the three modes $G_c = 0.30$ N/mm were taken. Since the three fracture energies are equal, the

difference term in Equation 4 vanishes and the mixed-mode exponent has no effect. The interface model used is thus a mode-independent bilinear model with constant fracture energy. The derivation in Section 3.3 is therefore independent of the mode mixity. The cohesive card, the impactor and the solver settings are given in Table 3.

Table 3. Cohesive interface card, impactor configuration and solver settings. Since the three fracture energies are equal, the Benzeggagh-Kenane exponent has no effect and the interface model is mode-independent. The three cohesive parameters are common to all six panels.

Group	Property	Symbol	Value	Unit
Cohesive interface	Penalty stiffness	$K_{nn} = K_{ss} = K_{tt}$	1×10^{6}	N mm^{-3}
	Nominal strength	$t_n^0 = t_s^0 = t_t^0$	73	MPa
	Mode I fracture energy	G_{Ic}	0.30	N mm^{-1}
	Mode II and III fracture energy	$G_{IIc} = G_{IIIc}$	0.30	N mm^{-1}
	Benzeggagh-Kenane exponent	η_{BK}	2.0	-
	Separation at initiation, t^0/K	δ_0	7.3×10^{-5}	mm
	Separation at failure, $2G_c/t^0$	δ_f	8.22×10^{-3}	mm
	Separation ratio δ_f/δ_0	r	112.6	-
Impactor	Radius	R_{imp}	8.0	mm
	Full-panel mass	m	5.5	kg
	Initial velocity	v_0	1.5609	m s^{-1}
	Full-panel impact energy	E_0	6.70	J
Contact and solver	Friction, general contact	μ	0.3	-
	Friction, cohesive pairs	μ_c	0.5	-
	Step time	T	30	ms
	Mass scaling target increment	Δt	2.5×10^{-8}	s
	Mesh seed, panel	h_e	1.25	mm
	Mesh seed, impactor	h_i	1.5	mm

2.3. Finite element model and solution

All solutions were carried out in Abaqus/Explicit. Since the panel has two planes of symmetry, a quarter region was modelled, and forces, masses, energies and areas were scaled to the full panel. Each sublaminate was meshed with eight-node SC8R continuum shell elements, and a single element per sublaminate was used through the thickness. The mesh seed size was held fixed at 1.25 mm in all configurations, and the number of elements rose with the arc length from 6000 in a1 to 9510 in a6. The impactor was modelled as a hemispherical rigid shell of 8 mm radius with R3D4 elements, and a point mass was assigned to its reference point. Symmetry conditions were applied on the apex plane and at mid-width, and the three translational degrees of freedom were

restrained on the radial edge and on the opposite edge. Since the SC8R element has no rotational degree of freedom, only translational conditions can be defined on the edges. At the impactor reference point only the vertical translation is free. The model, the mesh and the boundary conditions are summarised in Figure 2.

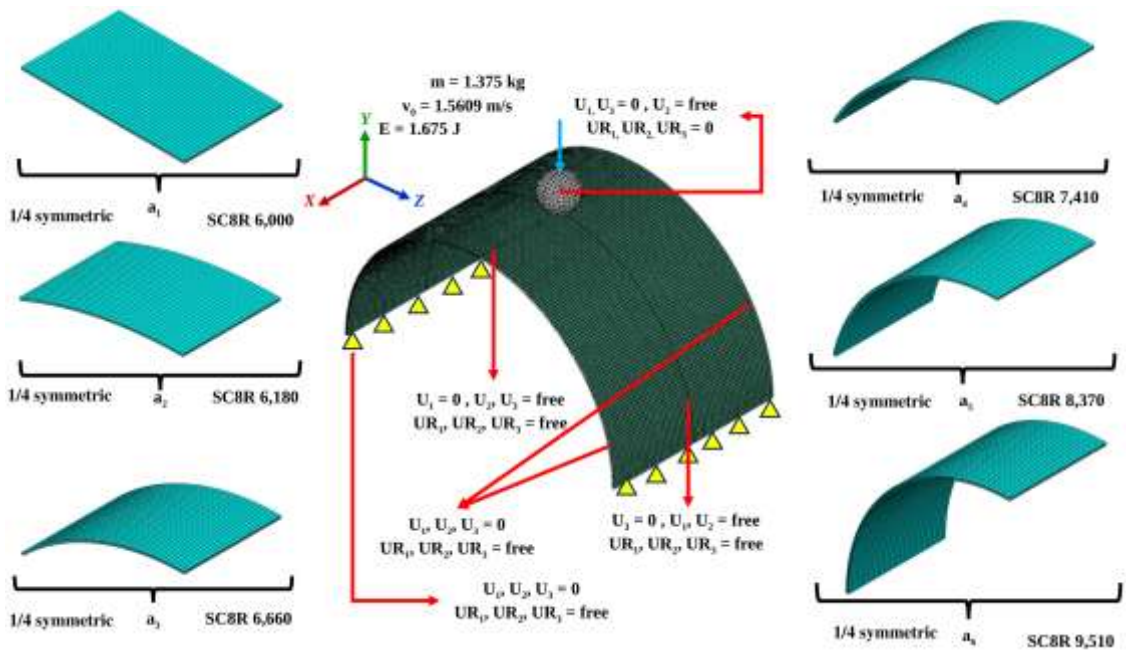

Fig. 2. Finite element model. SC8R continuum-shell mesh of the quarter model for the six configurations, the hemispherical rigid impactor, and the four boundary-condition groups covering the two symmetry planes, the clamped edges and the impactor reference point.

Contact was set up with the general contact algorithm, and the friction coefficient was taken as 0.3 between the impactor and the panel and 0.5 for the cohesive pairs. The impact energy was set according to the normalised energy criterion of the ASTM D7136 standard, which is proportional to the thickness. For a thickness of one millimetre it is 6.70 J on the full panel, which corresponds to an initial velocity of 1.5609 m/s for a mass of 5.5 kg. The quarter model carries a mass of 1.375 kg and an energy of 1.675 J at the same velocity. The solution time is 30 ms, and in all panels the contact ends before 22 ms.

In the script a target increment of 2.5×10^{-8} s was defined for semi-automatic mass scaling. The mass-scaling work of the solver is zero throughout the event in all six models. Since the target increment lies below the stable increment of the 1.25 mm element itself, the scaling did not act in any increment. The results are therefore solutions without mass scaling, and the energy balance gap in Section 4.2 cannot be attributed to mass scaling.

2.4. Processing of the outputs

The contact force was read from the contact reaction at the impactor reference point and scaled to the full panel. The impactor velocity, displacement and the absorbed energy were computed from the force history with the ASTM D7136 chain,

$$v(t) = v_0 - \frac{1}{m}\int_0^t F\ d\tau, \qquad w(t) = \int_0^t v\ d\tau, \qquad E(t) = \int_0^t F\ v\, d\tau \tag{5}$$

Here m is the full impactor mass and v_0 the initial velocity. Since there is no gravity in the finite element model, the gravity terms given by ASTM D7136 for the drop-weight set-up were not used. The contact duration

T_c is the time between the first instant at which the force departs from zero and the last instant at which it returns to zero. The coefficient of restitution e is the ratio of the rebound velocity at the end of contact to the initial velocity. The absorbed energy E_{abs} is the value of the energy computed with Equation 5 at the end of contact. The first damage load F_{dl} and its instant t_{dl} are defined as the load and the instant at which the first drop of five per cent of the peak value of the force is seen. This definition belongs to the force history and should not be confused with the instant at which the damage variables are first activated.

For interlaminar damage the cohesive damage variable CSDMG on the three interfaces was exported at the end of the event for every contact position of the quarter model and recorded together with the surface area belonging to each position. Full-panel areas were computed by giving a weight of one half to positions lying on a symmetry plane and one quarter at the corner, so that positions on the symmetry planes are not counted four times by mirroring. The area measures are defined in Section 3.4. The intralaminar damage variables and the stress fields are presented as images in Section 4.5.

2.5. Basis of validation

There is no experimental counterpart for these six panels, and no impact experiment on a curved woven T300/914 panel exists in the literature. The reliability of the model was therefore based on the literature at three levels. At the material level the card was taken from measurements made on the same woven T300/914 system at three strain rates [38]. At the formulation level the combination of the continuum shell element, Hashin intralaminar damage and surface-based cohesive interfaces was compared with drop-weight experiments on woven carbon/epoxy laminates, and the peak force error was found below 8 per cent and the difference in the delamination area measured by scanning 5.7 per cent [24]. It has been reported that the same framework predicted the delamination area within 20 per cent and the energy dissipation within 12 per cent for different stacking sequences [23], that in a woven glass composite over a wide energy range the peak force error remained below 11 per cent and the peak displacement error below 4 per cent [25], and that the interface-wise delamination distribution agreed with stereoscopic radiography when modelled together with intralaminar damage [5]. In a systematic comparison of combinations of damage criterion, evolution law and interface model it was shown that the impact response is determined by the evolution law and the delamination by the interface model, and that the Hashin criterion with linear evolution gives the energy dissipation with an error of 2.2 per cent [8]. In a joint study of the authors the same Hashin and cohesive framework was used together with impact experiments on filament-wound GFRP tubes [32]. These comparisons support the reliability of the formulation and of the material card, but they do not directly validate the curvature series, the predicted damage development and the numerical values solved here. The results are therefore presented as numerical findings, not as experimentally demonstrated behaviour.

At the geometry level the closest comparison is the semi-cylindrical woven shell study of Ferreira and co-workers [18]. There too the SC8R element and surface-based cohesive behaviour were used, and it was reported that the force and energy histories are not affected by the interface stiffness in the range 10^1 to 2.43×10^6 N/mm³, whereas the delamination prediction depends strongly on this parameter and the best agreement with experiment is obtained at 10^6 N/mm³. The penalty stiffness used here is also 10^6 N/mm³. In the same study the delamination area was defined with the 0.8 threshold of the damage variable, which is an example of the threshold practice addressed in Section 3.4. The results of Ferreira and co-workers are interpreted here in two ways. Global quantities such as the force, the displacement and the stiffnesses derived from them are insensitive to the cohesive card, and the results in Section 4.3 and Section 4.4 are at this level. The delamination areas, on the other hand, depend on the card, and the relation derived in Section 3.3 makes this dependence explicit through the parameter r of the card.

Mesh convergence was not performed in this study, and all models were solved with a single seed size of 1.25 mm. With the same SC8R and cohesive formulation, in the previous studies of the first author the global outputs converged much faster than the local interface area. In a three-mesh comparison the peak force changed by 1.3 per cent and the absorbed energy by 0.9 per cent from the medium to the fine mesh [35], whereas on the coarse mesh the deviation of the fully separated area was 21.4 per cent while that of the peak force was 3.8 per cent [35, 37]. These data show the behaviour of the formulation, they do not validate the mesh of the 1 mm

woven models here. For the sensitivity of the area measures to discretisation, a measurement resolution test was carried out on the exported damage fields and is given in Section 4.8. This test does not replace a mesh convergence study. The findings should therefore be read as the direction and relative magnitude of the change with curvature, not as absolute values.

3. Definitions of the measures and theoretical framework

The relations in the section fall into three classes. The stiffness, impulse and area measures are definitions. The mass spring relations and the cohesive law are taken over from the literature. The relation between the damage variable and the dissipated energy, on the other hand, is derived in this study. None of them contains a coefficient fitted to the results of the six panels.

3.1. Three stiffness measures

Three stiffnesses were defined on the loading branch of the curve of force against impactor displacement,

$$K_0 = \frac{\sum F_j w_j}{\sum w_j^2} \quad (0 < F_j \leq 0.35 F_{max}), \qquad K_{dl} = \frac{F_{dl}}{w_{dl}}, \qquad K_{sec} = \frac{F_{max}}{w_{max}} \tag{6}$$

The initial tangent stiffness K_0 is the least-squares slope of a line through the origin on the loading branch up to 35 per cent of the peak force, and it is an effective initial stiffness that carries the contact compliance and the inertial contribution of the panel together with the bending stiffness. The secant stiffness at first damage K_{dl} is the ratio of the force at the instant of the first significant force drop to the displacement at that instant. The secant stiffness at the peak K_{sec} is the ratio of the peak force to the maximum displacement. The first two measures describe the pre-damage behaviour, whereas the secant stiffness at the peak measures the effective spring constant of the damaged structure at the peak. The ratio K_{dl}/K_0 is a measure of the pre-damage hardening or softening, and the ratio K_{sec}/K_0 a measure of the total stiffness loss accumulated up to the peak.

3.2. Relations of the quasi-static regime

Olsson determined the regime of the response in low-velocity impact through the ratio of the impactor mass to the panel mass [34]. If the ratio is small, the response is controlled by the propagation of flexural waves and the contact duration is independent of the panel size. If the ratio is large, the waves reach the boundaries and return, the panel oscillates together with the impactor as a single mass spring system, and the response is quasi-static. Olsson's criterion for the large mass regime is that the impactor mass exceeds twice the panel mass. In the present series the ratio is between 232 and 367 (Table 1), and all six panels lie two orders of magnitude above the criterion.

In the quasi-static regime the impactor mass m stays in contact on a spring of effective spring constant K for half a period. For a linear spring the contact duration and the peak force are of the form

$$T_c = \pi \sqrt{\frac{m}{K}}, \qquad F_{max} = \sqrt{2 E_0 K} \tag{7}$$

Since the panel is not linear and accumulates damage up to the peak, Equation 7 is not a prediction. In this study the contact duration computed by substituting K_0 and K_{sec}, respectively, for K was compared with the measured T_c. Since K_0 is measured from the beginning of the loading branch and T_c from the time axis, the comparison made with K_0 is an independent test. Since K_{sec} is read from the peak of the same response, the comparison made with K_{sec} is not a prediction but a consistency test with the quasi-static mass spring description. The second expression of Equation 7, when used with K_{sec}, does not constitute an independent test either. When $K_{sec} = F_{max}/w_{max}$ is substituted,

$$\chi = \left(\frac{F_{max}}{\sqrt{2E_0K_{sec}}}\right)^2 = \frac{F_{max}\, w_{max}}{2E_0} \tag{8}$$

is obtained. χ is a pulse fullness coefficient that measures, at the peak, the fullness of the force against displacement curve relative to a linear spring passing through the same peak, and it is reported in this study only in this sense. The expression $\sqrt{(2E_0K_0)}$ for the peak force, on the other hand, is independent and was used in the test made with K_0. The transferred impulse is given with the coefficient of restitution,

$$I = m\, v_0(1+e), \qquad S = \frac{I}{F_{max}T_c} \tag{9}$$

and S is the shape factor of the force pulse. For a half-sine pulse $S = 2/\pi = 0.637$, for a triangle it is 0.5.

3.3. The cohesive damage variable and the dissipated energy

In surface-based cohesive behaviour the damage variable d is defined through the maximum effective separation reached, δ_{max},

$$d = \frac{\delta_f(\delta_{max}-\delta_0)}{\delta_{max}(\delta_f-\delta_0)}, \qquad \delta_0 = \frac{t^0}{K}, \qquad \delta_f = \frac{2G_c}{t^0} \tag{10}$$

and it reduces the interface stiffness to the value $(1-d)K$. This definition is a ratio of stiffness loss. In the bilinear law the energy density dissipated up to the point δ_{max} is obtained by subtracting the recoverable elastic energy at that point from the area under the loading curve,

$$D(\delta_{max}) = 1/2\, t^0\delta_{max} - 1/2\, t(\delta_{max})\delta_0 = G_c\, \frac{\delta_{max}-\delta_0}{\delta_f-\delta_0} \tag{11}$$

When δ_{max} is solved from Equation 10 and substituted into Equation 11, the dissipated energy fraction is written only in terms of d and the separation ratio r of the card,

$$\frac{D}{G_c} = \frac{d}{r-(r-1)\,d}, \qquad r = \frac{\delta_f}{\delta_0} = \frac{2G_cK}{(t^0)^2} \tag{12}$$

Equation 12 is a closed-form relation derived from the bilinear law, and it contains no fitting. In the limit $r = 1$ the curve falls onto the diagonal and the damage variable becomes directly the energy fraction. In real cards r is much larger than one, because the penalty stiffness is chosen large in order to suppress separation up to damage initiation. For the card used, $r = 112.6$ (Table 3). At this value $D/G_c = 0.0088$ for $d = 0.5$, 0.074 for $d = 0.9$, 0.47 for $d = 0.99$ and 0.90 for $d = 0.999$. At a position where the damage variable has reached one half, less than one per cent of the fracture energy has been dissipated. Since the G_c, K and t^0 values of the three modes are equal, the effective quantities are independent of the mode mixity and Equation 12 holds in the same form at every position. In a card carrying different parameters in different modes, r depends on the mode mixity and the relation must be evaluated together with the mixity ratio.

3.4. Area measures

With a_i the area and d_i the damage variable of position i on an interface, two area measures were defined,

$$A(d > x) = \sum_i a_i\; H(d_i - x), \qquad A_E = \sum_i a_i\, \frac{D(d_i)}{G_c} \tag{13}$$

The threshold area $A(d > x)$ is the quantity reported in the literature as the delamination area, and it depends on the chosen threshold. The energy-equivalent area A_E weights the area of each position with the dissipated energy fraction given by Equation 12. The product $G_c A_E$ equals the fracture energy dissipated at the interface, and A_E is therefore the interface area that would dissipate the same energy if it were fully separated, and it involves no choice of threshold. The threshold $x = 0.999$ was used as the fully separated area. At this threshold 90 per cent of the fracture energy has been dissipated according to Equation 12, and even the fully separated area is a lower bound in the energy sense. A_E lies between two bounds. For $r = 1$, $A_E = \Sigma a_i d_i$ and it is bounded by $A(d > 0)$, and as r grows only fully separated positions contribute and A_E descends to the fully separated area. Unlike the threshold areas, A_E depends not on an arbitrary choice but on the physical parameters of the card. The three measures, $A(d > 0.5)$, A_E and $A(d \geq 0.999)$, were computed in every panel separately for the three interfaces and as a total. The totals are the arithmetic sum of the three interfaces, not a union of projections.

4. Results

4.1. Global impact response

The force against time, force against displacement and energy against time histories are given for the six panels in Fig. 3 and their numerical counterparts in Table 4. The flat plate stands clearly apart from the series. Its peak force is the highest of the series at 1507.5 N, contact ends at 17.20 ms and the maximum displacement is the smallest of the series at 8.06 mm. In the five panels given curvature, the peak force drops to between 1155.9 and 1244.3 N, the contact duration extends to between 20.00 and 21.85 ms and the maximum displacement rises to between 8.56 and 9.09 mm. Relative to the flat plate the drop in the peak force is between 17.5 and 23.3 per cent and the extension of the contact duration between 16.3 and 27.0 per cent. The greater part of the change takes place at the transition from the flat plate to the first curvature level. The five curved panels stay within a narrow band among themselves and show no monotonic trend as f/a increases.

Table 4. Primary impact response of the six panels, scaled to the full panel. F_{dl} and t_{dl} are the load and the instant of the first drop of five per cent of the peak. e is the coefficient of restitution, E_{abs} the absorbed energy at the end of contact, $I = m\, v_0(1 + e)$ the transferred impulse and $S = I/(F_{max} T_c)$ the shape factor of the force pulse.

Panel	F_{dl} (N)	t_{dl} (ms)	F_{max} (N)	$t(F_{max})$ (ms)	w_{max} (mm)	T_c (ms)	e (-)	E_{abs} (J)	I (N s)	S (-)
a1	1176.8	3.20	1507.5	9.95	8.060	17.20	0.760	2.826	15.11	0.583
a2	765.8	2.25	1244.3	8.95	9.090	21.85	0.722	3.209	14.78	0.544
a3	792.9	2.20	1210.9	9.05	8.958	21.70	0.758	2.845	15.10	0.575
a4	854.4	2.15	1167.3	5.70	8.776	20.75	0.767	2.755	15.17	0.626
a5	838.4	2.20	1218.4	9.60	8.562	20.00	0.803	2.384	15.48	0.635
a6	903.8	3.20	1155.9	9.45	8.668	20.60	0.750	2.935	15.02	0.631

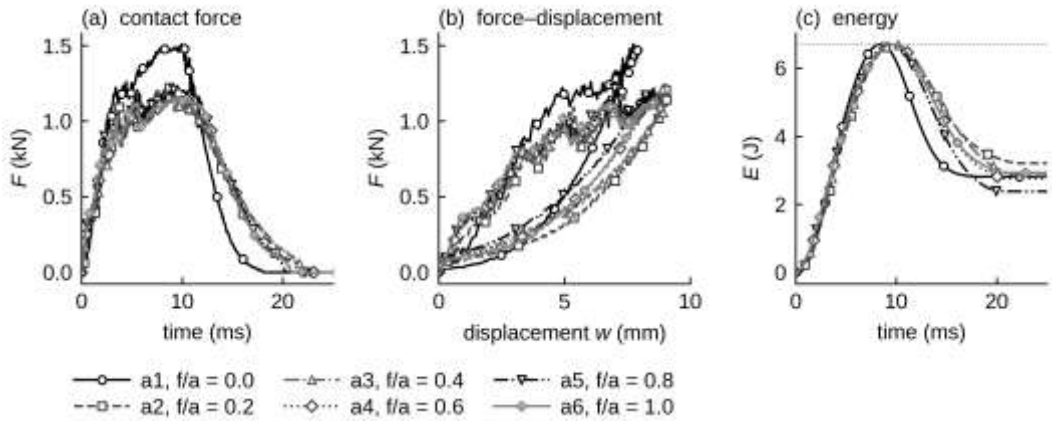

Fig. 3. Global impact response of the six panels, scaled to the full panel. (a) Contact force history. (b) Contact force against impactor displacement. (c) Energy history evaluated according to ASTM D7136, The horizontal line in (c) is the applied energy E_0 = 6.70 J.

The force histories are bell-shaped and carry pronounced oscillations on the loading branch. The first significant force drop is seen between 2.15 and 3.20 ms, well before the peak force. The drop load is highest in the flat plate at 1176.8 N, lowest in a2 at 765.8 N, and rises within the curved family towards a6 to 903.8 N. In panel a4 the peak force is read on an early spike at 5.70 ms, in the other panels the peak lies between 8.95 and 9.95 ms. The transferred impulse computed with Equation 9 stays between 14.78 and 15.48 N s in the six panels and its coefficient of variation is 1.4 per cent. The shape factor varies between 0.544 and 0.635 and its coefficient of variation is 5.7 per cent. In a4, a5 and a6 it stays between 0.626 and 0.635 and approaches the half-sine value of 0.637. The coefficient of variation of the peak force, by contrast, is 9.5 per cent. That the peak force falls while the area under the force pulse stays nearly constant means that the pulse lengthens and flattens. The absorbed energy is between 2.38 and 3.21 J and the coefficient of restitution between 0.722 and 0.803, and neither changes monotonically with curvature.

4.2. Energy balance and solution residual

The energy accounting is collected in Figure 4 and Table 5. The sum of the kinetic, internal and frictional energies at the end of the step is between 6.656 and 6.738 J in the six panels and accounts for the applied energy with a deviation smaller than 0.66 per cent. The ratio of the artificial hourglass energy to the internal energy stays between 0.026 and 0.044 at the highest value reached during the event. The mass-scaling work, the external work and the contact penalty work are zero in all six models. No element was deleted in any panel.

The solver's own total energy balance, on the other hand, is between 7.096 and 9.246 J at the end of the step. Its difference from the sum of the three components is between 0.440 and 2.555 J, corresponds to 6.6 to 38.1 per cent of the applied energy and grows with curvature. The possible effect of this residual on the results was tested in three ways from the existing energy histories. The sum of the kinetic, internal and frictional energies matches the applied energy within 0.9 per cent not only at the end of the step but at every output instant (Fig. 4b). Since this sum stays constant while the residual grows at the same time, the term forming the residual is not drawn from the mechanical energy of the impactor and the panel. Up to the instant of first damage the residual is below 0.03 J, and this value is less than 0.4 per cent of the applied energy. At the instant of peak force it has reached 15 to 59 per cent of its final value, and the remainder accumulates on the unloading branch. While the residual grows together with curvature (correlation coefficient 0.93) and with the number of elements (0.85), it shows no clear relation with the interface damage area (0.52), the intralaminar damage energy (−0.44) and the energy-equivalent area (0.59), and it therefore cannot be interpreted as an unreported damage dissipation. The three observations together show that the initial and first damage stiffnesses are independent

of the residual and that the peak quantities were measured when at most 59 per cent of the residual had accumulated. The source of the residual, however, could not be identified in this study. Since the mass-scaling work is zero, it cannot be attributed to mass scaling, and since the exported viscous dissipation output does not agree with the magnitude of the residual, it has not been attributed to that either. The residual is taken up again in Section 5.4 as a limit of scope.

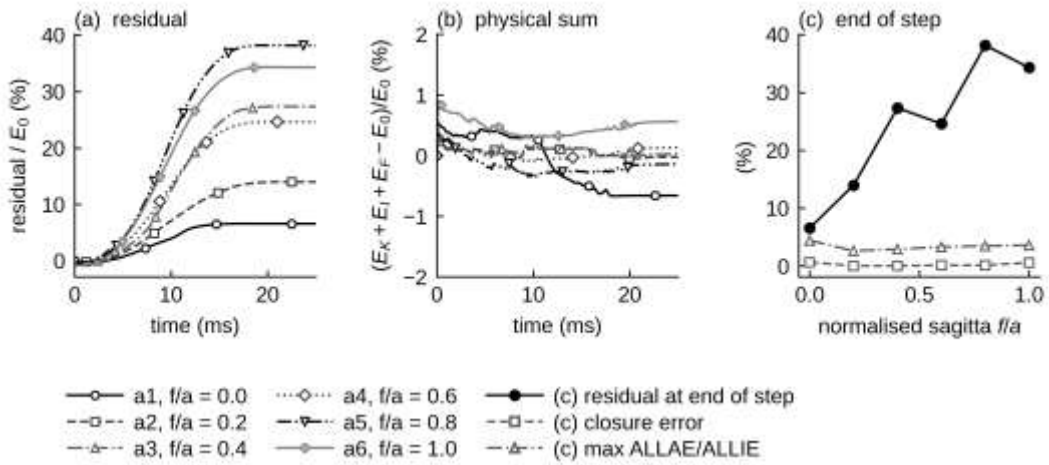

Fig. 4. Energy accounting. (a) Residual of the solver total energy balance with respect to the sum of the kinetic, internal and frictional energies, as a fraction of the applied energy. (b) Deviation of the sum of the kinetic, internal and frictional energies from the applied energy during the whole step. (c) Residual at the end of the step, closure error of the three components and the maximum ratio of artificial to internal energy, against the normalised sagitta.

Table 5. Mesh and numerical quality indicators. Element counts are for the quarter model at the common 1.25 mm seed. The closure error is the deviation of ALLKE + ALLIE + ALLFD from the applied energy at the end of the step. The residual is the part of the solver total energy balance not covered by those three terms. ALLMW is the mass-scaling work reported by the solver. The table reports internal consistency at a fixed seed size, not a mesh convergence study.

Panel	SC8R elements	Closure error (%)	max ALLAE/ALLIE (-)	Residual (J)	Residual / E_0 (%)	ALLMW (J)	Deleted elements
a1	6000	0.66	0.044	0.440	6.6	0	0
a2	6180	0.03	0.026	0.936	14.0	0	0
a3	6660	0.03	0.029	1.831	27.3	0	0
a4	7410	0.14	0.033	1.648	24.6	0	0
a5	8370	0.13	0.035	2.555	38.1	0	0
a6	9510	0.57	0.036	2.296	34.3	0	0

In the check made during the review, it was found that the post-processing script that derives the impactor velocity, displacement and energy from the force history contained the gravity terms written in ASTM D7136 for the drop-weight set-up. There is no gravity load in the finite element model, and the external work is zero in all six models. In the first version these terms increased the maximum displacement by 0.36 to 0.50 mm and the peak of the energy curve by 0.45 to 0.52 J, and caused the ASTM curve to exceed the applied energy by 7 per cent and the force impulse to come out 7.5 to 9.5 per cent higher than the momentum impulse. All quantities were recomputed without gravity with Equation 5. In the corrected chain the ASTM curve peaks at 6.700 J in all six panels, the difference between the force impulse and $m\,v_0(1 + e)$ is below 0.1 per cent, and the work done up to the peak force stays between 5.00 and 6.70 J and does not exceed the applied energy. The correction did

not change the force history, the contact duration and the peak force, and it changed the displacement-dependent quantities, w_{max}, K_{dl}, K_{sec}, the coefficient of restitution and the absorbed energy. Table 4, Table 6 and Table 7 and all values depending on them are taken from the corrected chain.

4.3. Three stiffness measures

The three stiffnesses defined by Equation 6 are given in Fig. 5 and Table 6. The initial tangent stiffness increases monotonically with curvature, rising from 188.9 N/mm to 328.5 N/mm, an increase of 74 per cent. The increase is the expected consequence of curvature coupling the membrane and bending behaviour in the cylindrical shell. The secant stiffness at the peak behaves in the opposite direction. K_{sec}, which is 187.0 N/mm in the flat plate, falls to 136.9 N/mm at the first curvature level and stays between 133.0 and 142.3 N/mm in the five curved panels. The drop relative to the flat plate is between 23.9 and 28.9 per cent. The two stiffness measures change in opposite directions in the same series.

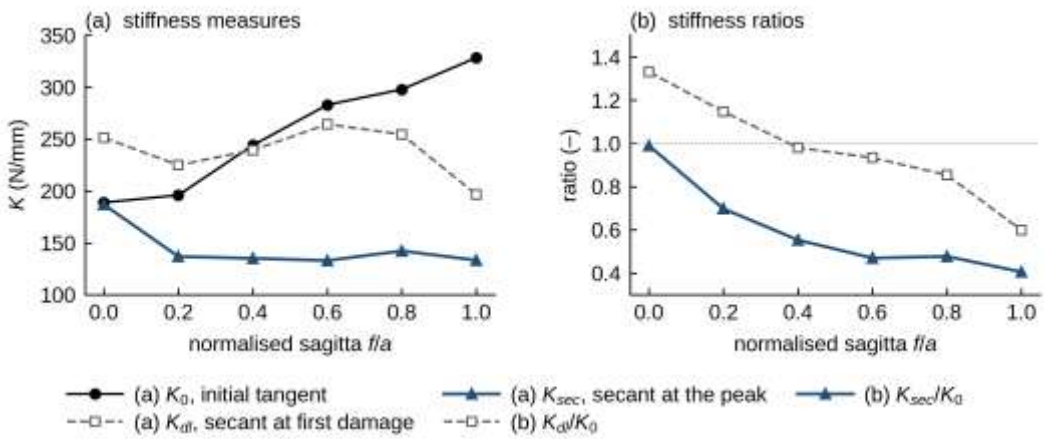

Fig. 5. Stiffness measures against the normalised sagitta. (a) Initial tangent stiffness K_0, secant stiffness at first damage K_{dl} and secant stiffness at the peak K_{sec}. (b) The ratios K_{dl}/K_0 and K_{sec}/K_0, which measure the pre-damage hardening or softening and the total stiffness loss up to the peak.

Table 6. Stiffness measures of Equation 6 and their ratios. K_0 is the initial tangent stiffness over $0 < F \leq 0.35$ F_{max}, K_{dl} the secant stiffness at the first damage load and K_{sec} the secant stiffness at the peak.

Panel	K_0 (N mm^{-1})	K_{dl} (N mm^{-1})	K_{sec} (N mm^{-1})	w_{dl} (mm)	K_{dl}/K_0 (-)	K_{sec}/K_0 (-)
a1	188.9	251.4	187.0	4.68	1.33	0.99
a2	196.0	225.0	136.9	3.40	1.15	0.70
a3	244.2	239.4	135.2	3.31	0.98	0.55
a4	283.1	264.4	133.0	3.23	0.93	0.47
a5	298.0	254.6	142.3	3.29	0.85	0.48
a6	328.5	196.6	133.4	4.60	0.60	0.41

Table 7. Quasi-static description of Equation 7. $T_{c,pred} = \pi\sqrt{(m/K_{sec})}$ is evaluated with the secant stiffness at the peak and is a consistency check, not a prediction. $\pi\sqrt{(m/K_0)}$ and $\sqrt{(2E_0K_0)}$ are the same expressions evaluated with the initial stiffness. χ is the pulse fullness coefficient of Equation 8.

Panel	T_c (ms)	$T_{c,pred}$ (ms)	Deviation (%)	$\pi\sqrt{(m/K_0)}$ (ms)	F_{max} (N)	$\sqrt{(2E_0K_0)}$ (N)	χ (-)
a1	17.20	17.04	-1.0	16.95	1507.5	1591	0.907
a2	21.85	19.91	-8.9	16.64	1244.3	1621	0.844
a3	21.70	20.04	-7.7	14.91	1210.9	1809	0.810
a4	20.75	20.20	-2.6	13.85	1167.3	1948	0.764
a5	20.00	19.53	-2.3	13.50	1218.4	1998	0.779
a6	20.60	20.18	-2.1	12.85	1155.9	2098	0.748

The secant stiffness at first damage shows where the divergence between the two measures begins. In the flat plate $K_{dl}/K_0 = 1.33$, and the plate hardens before first damage. The hardening is the consequence of the membrane stress that develops in a supported thin plate as the deflection reaches several times the thickness. In the flat plate first damage is seen at a deflection of 4.68 mm, at 4.7 times the thickness. The ratio falls monotonically with curvature, reaches one at a3 and recedes to 0.60 in the half cylinder. The curved shell softens before first damage. From a2 to a5 first damage is seen at deflections of 3.23 to 3.40 mm, earlier than in the flat plate, it shifts to 4.60 mm in the half cylinder, and by then the curved shell has fallen below its initial stiffness. The total loss accumulated up to the peak, K_{sec}/K_0, is 0.99 in the flat plate and between 0.41 and 0.70 in the curved panels. The panel with the highest initial stiffness retains 41 per cent of its initial stiffness when it reaches the peak.

To test the interpretation beyond the indirect stiffness data, the stress histories at probe points placed along the arc and along the axis in sublaminate 2, at a depth of 0.375 mm from the impacted face and 0.125 mm above the mid-plane, were used. A1 is the arc point nearest to the contact point, and A2, A3 and A4 advance along the arc towards the support. Z1 to Z4 lie on the axial line passing through the contact point. Since the probe points represent a single position through the thickness, they carry part of the bending stress in addition to the membrane stress and should be read as a stress indicator, not as a resultant force. Since the element directly beneath the contact point was damaged in the first milliseconds, the data of that point were not used. In the flat plate the hoop stress is tensile at all points along the arc from the beginning and grows with the load (Fig. 6a and Fig. 6b). The mean of the outer arc points is 84.9 MPa at the instant of first damage and 140.7 MPa at the instant of peak force. This points to the plate carrying membrane tension over the whole span and to the pre-damage hardening in Table 6 coming from this load path. In the curved panels the point A1 near the contact carries a hoop compression of 8.4 to 24.1 MPa in the first 0.5 to 0.8 ms. The compression is the expected sign of the contribution of curvature to the initial stiffness. The stress at A1 turns permanently into tension between 1.4 and 3.6 ms, and the reversal takes place near the instants of first damage (2.15 to 3.20 ms). At the outer arc points, on the other hand, the hoop stress stays small throughout the event. The mean at the instant of peak force is 31.1 MPa in a2 and 2.5 MPa in a6, and it is 4.5 to 57 times below that of the flat plate (Fig. 6c). The stresses on the axial line, by contrast, are of the same order in the six panels at 83 to 126 MPa, so the quantity that separates the panels is the load carrying in the hoop direction, not in the axial direction. The stress distribution is consistent with the interpretation that the additional load the curved shell carries by hoop compression around the contact is lost as the dent develops, and that the span-wide membrane tension that hardens the flat plate does not develop in the curved shell. Since the probe points are limited to a single position through the thickness, the membrane and bending shares could not be separated from each other.

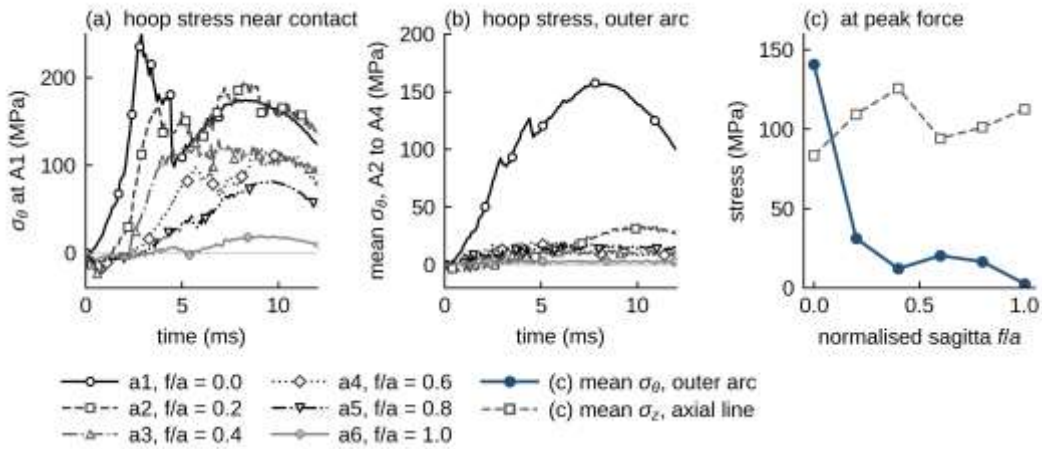

Fig. 6. Hoop stress along the curved direction in sublaminate 2, 0.125 mm above the mid-plane. (a) Hoop stress at probe A1, the arc probe nearest to the contact point. (b) Mean hoop stress of the outer arc probes A2 to A4. (c) Mean hoop stress of the outer arc probes and mean axial stress of the axial probes Z1 to Z4 at the instant of peak force, against the normalised sagitta. The dotted horizontal line marks zero stress.

4.4. Quasi-static test

The contact duration computed with Equation 7 is compared with the measured contact duration in Fig. 7 and Table 7. In the independent test made with K_0 the expression predicts a contact duration that falls from 17.0 ms to 12.8 ms, whereas the measured duration rises from 17.2 ms to above 20 ms. The initial stiffness does not give correctly even the direction of the change of the contact duration with curvature. The same expression, when computed with K_{sec}, is consistent with the measured value within 8.9 per cent in the six panels. The difference is 1.0 per cent in the flat plate, 2.1 to 2.6 per cent in a4, a5 and a6 and 7.7 to 8.9 per cent in a2 and a3, and the computed duration stays below the measured one in all six panels. Since K_{sec} is read from the response itself, this consistency is not a prediction. What it shows is that the measured contact duration is consistent with the quasi-static description in which the impactor performs a half-period oscillation on the effective spring constant at the peak.

For the peak force, the expression $\sqrt{(2E_0K_0)}$ built with K_0 predicts a peak force that rises from 1591 N to 2098 N. The measured force, however, falls from 1507 N to 1156 N. The expectation that the stiffness increase raises the peak force reads the series in the opposite direction when it is built on the initial stiffness. The counterpart of the same expression built with K_{sec} is not an independent test by virtue of Equation 8, and the pulse fullness coefficient χ is reported in its place (Fig. 7b). χ is 0.907 in the flat plate and between 0.748 and 0.844 in the curved panels and falls with curvature. While the force against displacement curve of the flat plate stays close to a linear spring up to the peak, the curve of the curved panels sags further below the secant line at the peak. This is the counterpart, in the shape of the force against displacement curve, of the pre-damage softening in Table 6.

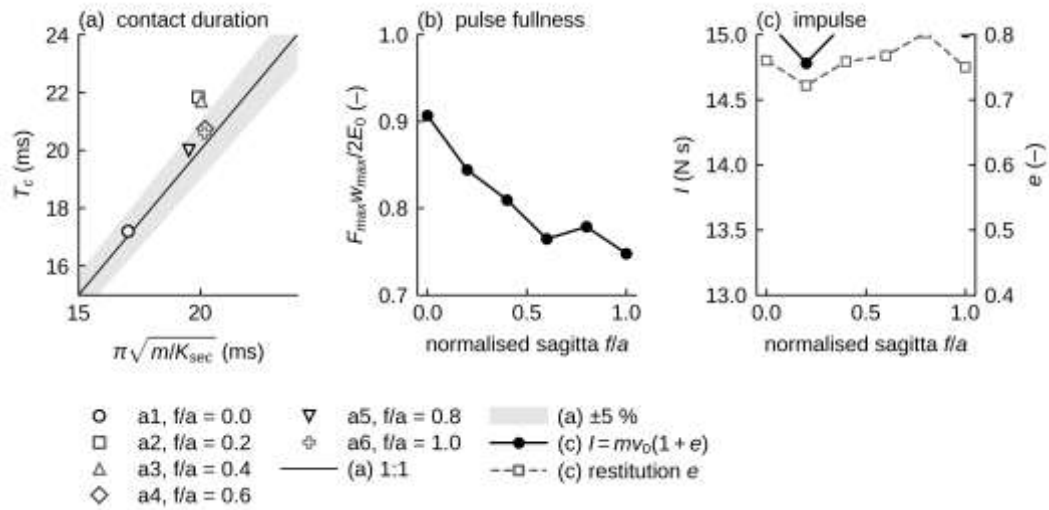

Fig. 7. Quasi-static description. (a) Measured contact duration against $\pi\sqrt{(m/K_{sec})}$. The solid line is the 1:1 line and the shaded band marks ±5 %. (b) Pulse fullness coefficient $\chi = F_{max}w_{max}/2E_0$ of Equation 8 against the normalised sagitta. (c) Transferred impulse $I = m\ v_0(1 + e)$ and coefficient of restitution against the normalised sagitta.

The transferred impulse is nearly constant along the series, as shown in Fig. 7c, and its coefficient of variation is 1.4 per cent. The product $F_{max}T_c$, by contrast, is 25.9 N s in the flat plate and between 23.8 and 27.2 N s in the curved panels. The force pulse, lengthened and flattened by curvature, transfers a nearly constant impulse over a longer time. That the shape factor approaches the half-sine value in the panels of high curvature is consistent with the quasi-static mass spring description, since the contact force of a linear spring is a half sine.

4.5. Intralaminar damage

The Mises stress and the four Hashin damage variables on the top and bottom faces at the end of the event are given in Fig. 8 and Fig. 9. In the images the horizontal axis is the curvature direction *x* and the vertical axis the width direction *z*. The dominant intralaminar mode in every panel and on both faces is the 2-direction tension mode. This mode forms an ellipse elongated in the curvature direction around the contact point, and the shape of the ellipse is similar in the six panels. The effect of curvature is seen in the other three modes. On the top face the fibre compression mode is a point only at the contact point in the flat plate, whereas in the curved panels it turns into a thin line passing through the contact point and extending in the width direction. The line runs along the generator of the cylinder and shows that in the curved shell the dent beneath the contact elongates along the generator. On the top face the fibre tension mode is activated in a single region beneath the contact in the flat plate, and from a4 onwards in separate regions on both sides of the contact point along the generator. On the bottom face the fibre tension mode settles in all panels into a single region beneath the contact point elongated along the generator, while the fibre compression mode appears from a3 onwards and after a4 spreads into two symmetric side regions along the generator. On the bottom face the 2-direction compression mode is not activated in any panel. The distribution of intralaminar damage shows that in the flat plate the damage concentrates around the contact point, whereas in the curved shell the dent elongates along the generator and the load is carried over a longer line. Intralaminar damage did not progress to element deletion in any panel.

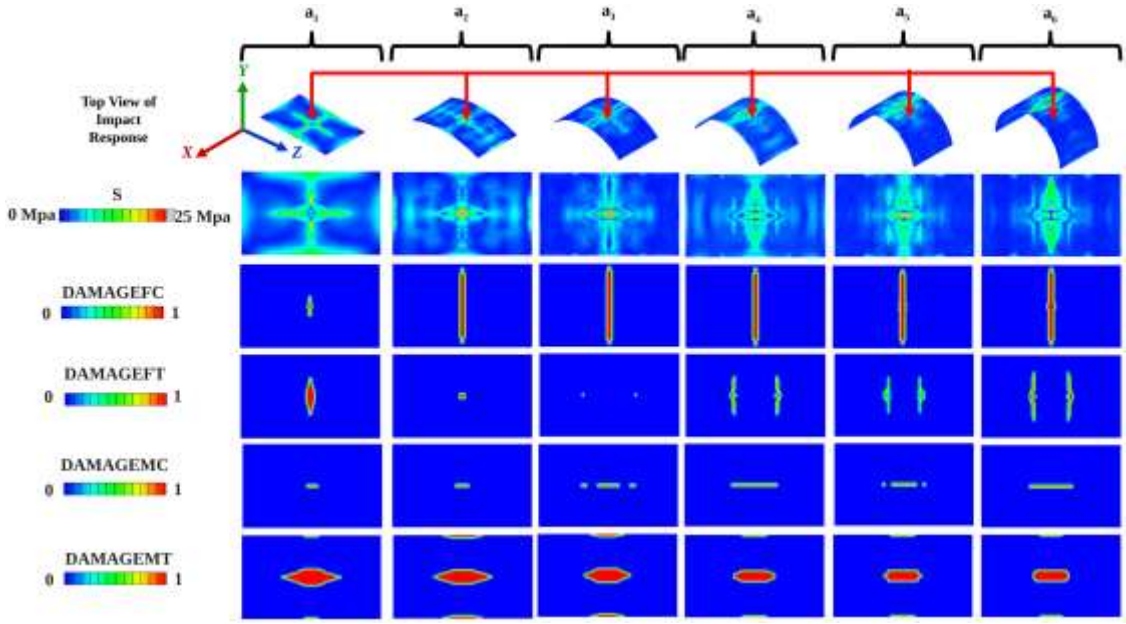

Fig. 8. Top view of the impacted face at the end of the event. Mises stress and the four Hashin damage variables, fibre compression (DAMAGEFC), fibre tension (DAMAGEFT), 2-direction compression (DAMAGEMC) and 2-direction tension (DAMAGEMT), for the six panels. Contour ranges are common to all panels.

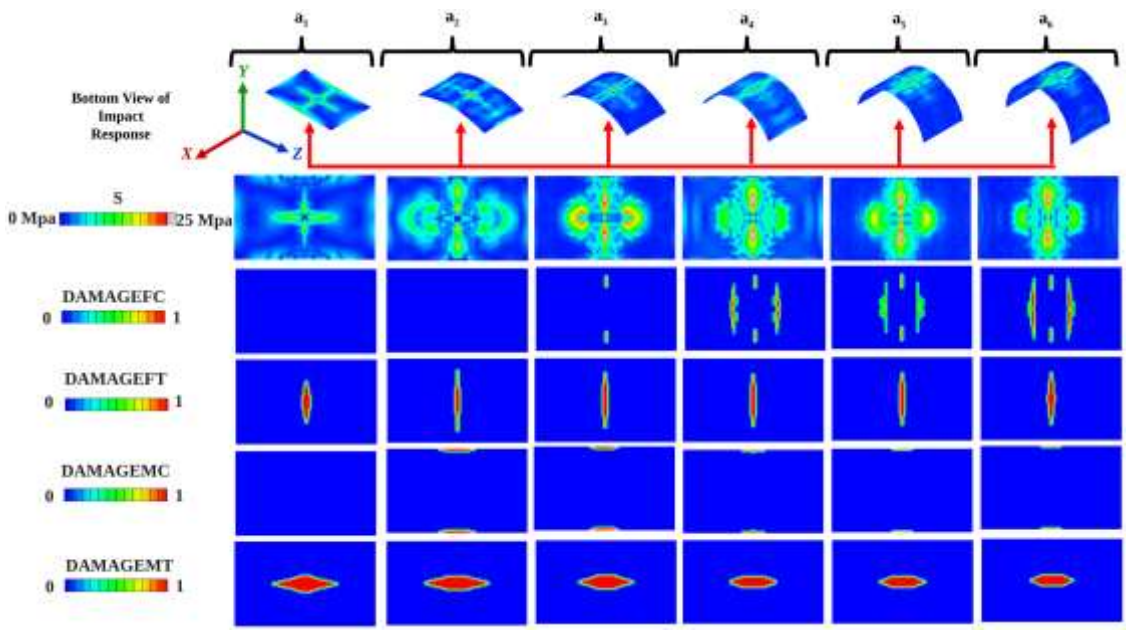

Fig. 9. Bottom view of the back face at the end of the event. Mises stress and the four Hashin damage variables for the six panels. Contour ranges are common to all panels.

4.6. Interlaminar damage

The cohesive damage variable on the three interfaces is shown through the thickness in Fig. 10. In all panels the damage settles beneath the contact point into a region elongated in the arc direction and narrow in the width direction. The image gives the distribution of the damage variable, not the distribution of the dissipated energy. The difference between the two is shown with Equation 12 in Fig. 11a. For the separation ratio of the card, r = 112.6, the curve stays far below the diagonal up to d = 0.9, and 90 per cent of the dissipated energy is squeezed into the range d > 0.999. Even a position that has reached 99 per cent of the stiffness loss has dissipated less than half of the fracture energy.

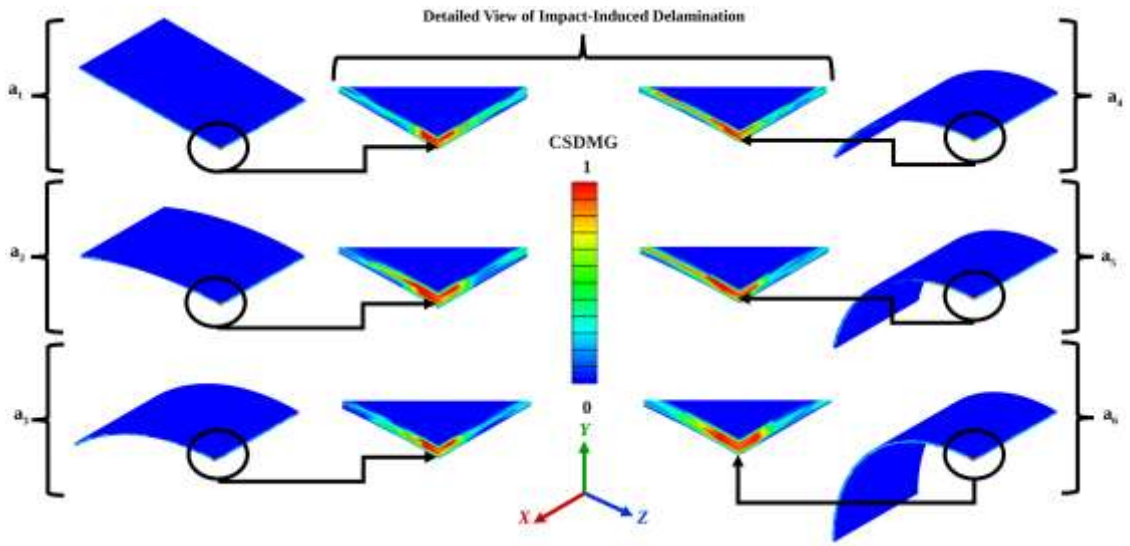

Fig. 10. Cohesive damage variable CSDMG on the three interfaces at the end of the event, viewed through the thickness for the six panels. The colour bar is common to all panels.

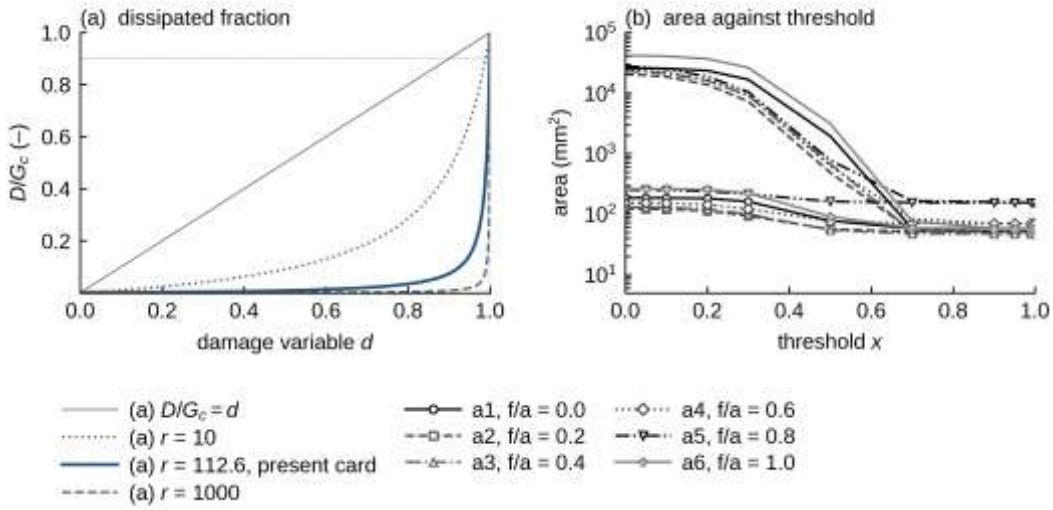

Fig. 11. Meaning of the cohesive damage variable. (a) Dissipated fraction D/G_c against the damage variable d from Equation 12, for the separation ratio of the card used here, $r = 112.6$, and for $r = 10$ and $r = 1000$. The diagonal is the assumption that the damage variable measures dissipated energy. The thin guide lines mark $d = 0.5$ and $d = 0.999$, at which 0.9 % and 90 % of G_c are dissipated. (b) Threshold area $A(d > x)$ and energy-equivalent area $A_E(d > x)$ of the six panels against the threshold, summed over the three interfaces. Lines without markers are $A(d > x)$ and lines with markers are $A_E(d > x)$.

Fig. 11b shows the dependence of the threshold area on the threshold. At the zero threshold the area is between 20.7×10^3 and 41.7×10^3 mm², that is, the damage variable is greater than zero over a large part of the interface. The area falls slowly up to the 0.3 threshold, by more than an order of magnitude between 0.3 and 0.7, and approaches the fully separated area above 0.9. The areas of the thresholds between 0.95 and 0.9999 are identical in the six panels, and the 0.9 threshold is larger by 4.5 mm² only in a5, because the damage variable saturates at unity at the separated positions. The energy-equivalent area defined by Equation 13, by contrast, does not depend on the threshold to this extent. The share of A_E coming from positions above the threshold falls to 35 to 65 per cent of the total A_E when the threshold is raised from zero to 0.5, and to 22 to 62 per cent when it is raised to 0.999. The last ratio means that the fully separated region carries only 22 to 62 per cent of the energy dissipated at the interface. The remaining share comes from the band in which the damage variable stays below 0.999 and which appears on no map of full separation.

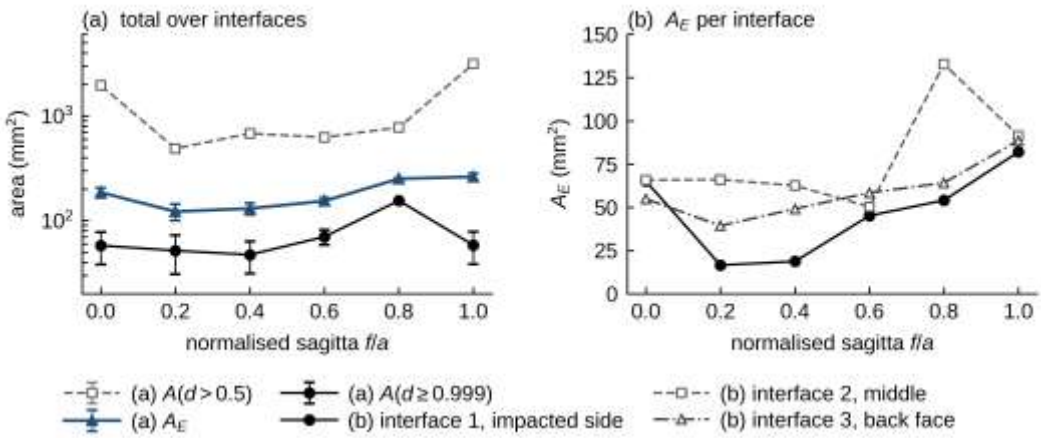

Fig. 12. Delamination measures against the normalised sagitta, on the mirrored full panel. (a) Threshold area $A(d > 0.5)$, energy-equivalent area A_E and fully separated area $A(d \geq 0.999)$, summed over the three interfaces. (b) Energy-equivalent area of each interface. The error bars in (a) are ± one coefficient of variation of the resolution test in Table 9.

Table 8. Interlaminar damage at the end of the event on the mirrored full panel. $A(d > 0.5)$ is the threshold area at one half, A_E the energy-equivalent area of Equation 13 and $A(d \geq 0.999)$ the fully separated area. $G_c A_E$ is the interfacial fracture energy dissipated. Interface 1 is on the impacted side.

Panel	$A(d > 0.5)$ (mm²)	A_E (mm²)	$A(d \geq 0.999)$ (mm²)	$A(d > 0.5)/A_E$ (-)	$A_E/A(d \geq 0.999)$ (-)	$G_c A_E$ (mJ)	A_E, interface 1 (mm²)	A_E, interface 2 (mm²)	A_E, interface 3 (mm²)
a1	1955	185.8	57.8	10.5	3.21	55.7	65.2	65.8	54.9
a2	487	122.0	51.7	4.0	2.36	36.6	16.6	66.0	39.4
a3	679	130.5	47.2	5.2	2.76	39.1	18.7	62.6	49.1
a4	624	153.9	70.0	4.1	2.20	46.2	45.2	50.3	58.4
a5	777	251.0	155.1	3.1	1.62	75.3	54.0	132.8	64.1
a6	3142	262.2	58.3	12.0	4.49	78.6	82.0	91.4	88.7

The variation of the three measures with curvature is given in Fig. 12a and Table 8. The energy-equivalent area is between 122.0 and 262.2 mm², it starts at 185.8 mm² in the flat plate, falls to its lowest value at a2 and rises towards the half cylinder. The fracture energy dissipated at the interface is accordingly between 36.6 and 78.6 mJ and is 1.1 to 3.2 per cent of the absorbed energy. The area of the 0.5 threshold is 3.1 to 12.0 times A_E, whereas the fully separated area is 1.62 to 4.49 times below A_E. The two extreme values are seen in the flat plate and in the half cylinder. In these two panels the area of the 0.5 threshold rises to 1955 and 3142 mm², three to six times that of the curved panels, while the fully separated area, at 57.8 and 58.3 mm², is at the same level as the other panels. The two thresholds produce opposite rankings for the same two panels. A comparison that reads the flat plate and the half cylinder with the 0.5 threshold finds these panels the most damaged, whereas a comparison that reads them with the 0.999 threshold finds a5 the most damaged. The energy-equivalent area involves no choice of threshold. Within the resolution uncertainty of Section 4.8, a5 and a6 form the highest and a2 and a3 the lowest group, and a1 and a4 lie between these two groups. The ranking within the groups lies inside the uncertainty band and has not been interpreted.

The distribution among the interfaces is given in Fig. 12b. In the flat plate the three interfaces take approximately equal shares of 54.9 to 65.8 mm². In the shallow curved panels a2 and a3 the share of the interface near the impacted face falls to 16.6 and 18.7 mm² and the middle interface becomes dominant. From a4 onwards the interface near the impacted face grows again, in a5 the middle interface alone carries half of the total with

132.8 mm², and in the half cylinder the three interfaces become equal again with 82.0 to 91.4 mm². That the through-thickness distribution changes with curvature in this way suggests that the through-thickness profile of the shear stress changes with curvature. The relief of the interface near the impacted face at shallow curvature is consistent with the compression zone beneath the contact in the curved shell passing into membrane compression without carrying shear stress. This interpretation cannot be verified without extracting the through-thickness stress profile and is given as a proposed explanation. The areas per interface are between 16.6 and 132.8 mm², and the resolution uncertainty of Section 4.8 is larger for them than for the total areas, so the shares among the interfaces should be read as trends.

4.7. Time axis

The development of the fully separated area in time is given in Fig. 13 together with the force history. Separation begins in the six panels between 0.7 and 1.3 ms, while the force is between 345 and 408 N. The initiation force is below one third of the peak force and well before the first significant force drop. The instant at which the force reaches half of its peak value is between 1.60 and 2.05 ms in the six panels. In panels a1, a2, a3 and a6 the whole of the fully separated area at the end of the event has formed before this instant, and in these four panels the fully separated area did not grow at all after half of the load. In a4, 92 per cent and in a5, 47 per cent of the area forms before this instant. The remainder is added in a single step at 1.9 ms in a4, and in a5 step by step up to 7.1 ms while the load rises towards the peak. That a5 has the largest fully separated area of the series results from this late growth.

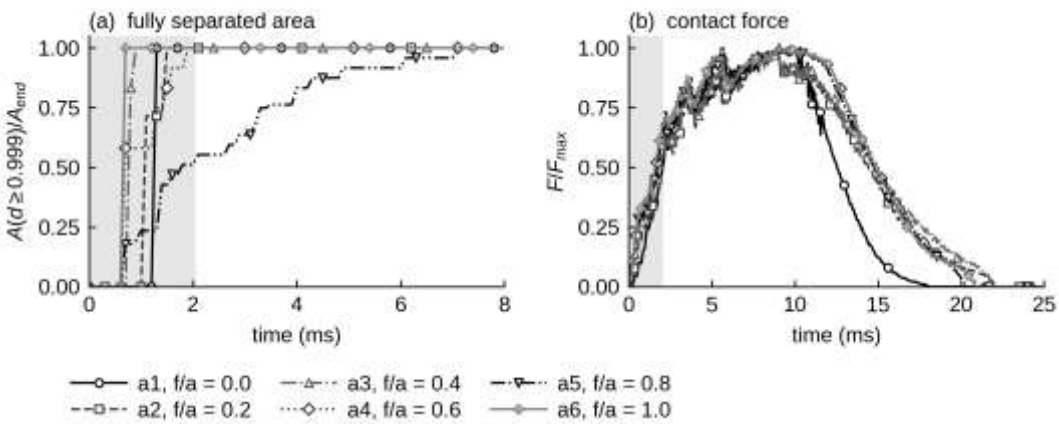

Fig. 13. Time axis of delamination. (a) Fully separated area relative to its value at the end of the event, from the quarter-model history. (b) Contact force relative to its peak. The shaded band marks the interval in which the force is below one half of its peak.

The first significant drop in the force history, on the other hand, is seen between 2.15 and 3.20 ms, 1 to 2 ms after the onset of full separation. The damage load read from the force history and the load at which interface separation begins are not the same quantity. In the series the former is between 766 and 1177 N and the latter between 345 and 408 N. Comparisons that use the force drop as the delamination threshold load should take this difference into account.

4.8. Resolution and card sensitivity of the area measures

In order to place a bound on the sensitivity of the area measures to discretisation without a new solution, a measurement resolution test was carried out on the exported damage fields. The positions of each interface were taken at every second position in the arc and axial directions, each retained position was given the area of four positions, and the three measures were recomputed for the four possible starting offsets. The procedure

corresponds to a sampling at 2.5 mm spacing instead of 1.25 mm. The coefficient of variation among the offsets gives the resolution uncertainty of the measure itself and is collected in Table 9. The coefficient of variation of the fully separated area is between 16.3 and 40.5 per cent except for a5, because the fully separated region covers only 30 to 100 positions at 1.25 mm spacing. That of the energy-equivalent area is between 1.3 and 17.6 per cent, and that of the area of the 0.5 threshold between 1.8 and 4.5 per cent. Because it covers a wide region, the most stable measure is the area of the 0.5 threshold, but, as shown in Section 4.6, this measure carries no energy meaning. The energy-equivalent area is clearly more stable than the fully separated area. The test does not predict the damage area that a new mesh would give, it only gives the uncertainty coming from the measurement of the existing field.

Table 9. Sensitivity of the area measures. The coefficients of variation are obtained by sampling every second position of the exported damage field in both surface directions, which corresponds to a 2.5 mm spacing instead of 1.25 mm, over the four possible offsets. The last four columns give the energy-equivalent area evaluated from the same damage field with other separation ratios r in Equation 12.

Panel	A_E (mm²)	CV of A_E (%)	CV of $A(d > 0.5)$ (%)	CV of $A(d \geq 0.999)$ (%)	A_E, $r = 10$ (mm²)	A_E, $r = 30$ (mm²)	A_E, $r = 300$ (mm²)	A_E, $r = 1000$ (mm²)
a1	185.8	10.9	2.4	34.3	1415	530	106	72
a2	122.0	17.6	4.2	40.5	806	312	78	60
a3	130.5	12.5	2.7	33.7	939	355	79	57
a4	153.9	7.3	4.5	16.3	969	381	102	80
a5	251.0	1.3	2.8	2.5	1182	510	191	166
a6	262.2	7.9	1.8	34.3	2218	811	135	81

The dependence of the energy-equivalent area on the cohesive card appears through the parameter r of Equation 12. The variation of A_E with r for the same damage field is given in the last columns of Table 9 and in Fig. 14b. At $r = 10$, A_E is between 806 and 2218 mm² and approaches the area of the 0.5 threshold, at $r = 1000$ it is between 57 and 166 mm² and descends to the fully separated area. This is the numerical counterpart of the two bounds in Section 3.4. The ranking changes partly with r. a2 and a3 are in the lowest group at all values of r, whereas the highest position is held by a6 up to $r = 112.6$ and by a5 at $r = 300$ and above. The comparison is a reweighting of the same damage field with different cards and does not cover the fact that the damage field itself would change when the card changes. What it shows is that A_E depends not on an arbitrary choice like the threshold areas but on the measurable parameters of the card.

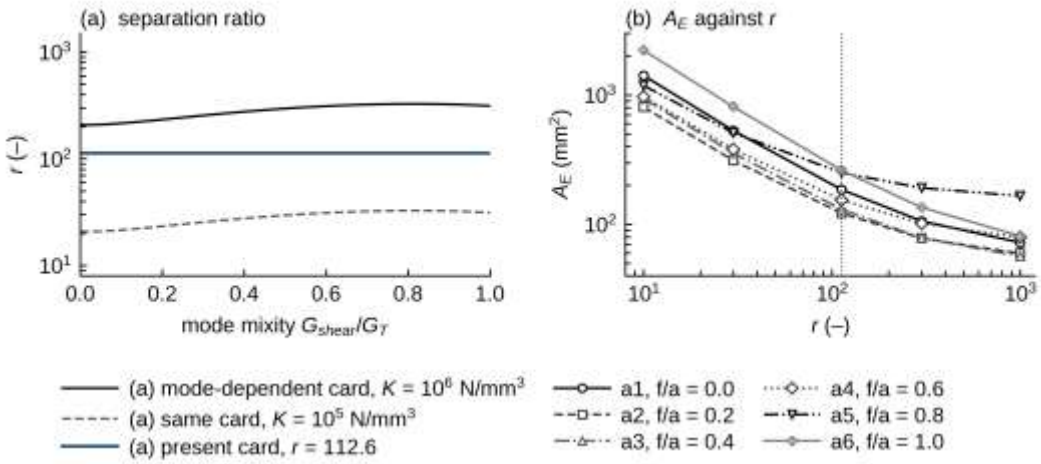

Fig. 14. Dependence on the cohesive card. (a) Separation ratio r against the mode mixity G_{shear}/G_T for a mode-dependent bilinear card with the Benzeggagh-Kenane law of Equation 14 (t_n^0 = 50 MPa, t_s^0 = 80 MPa, G_{Ic} = 0.26 N/mm, G_{IIc} = 1.002 N/mm, η_{BK} = 1.45) at two penalty stiffnesses, together with the mode-independent card of the present study. (b) Energy-equivalent area of the six panels evaluated from the same damage fields with different separation ratios. The dotted vertical line marks r = 112.6.

5. Discussion

5.1. Mechanism of the concurrent stiffness increase and force decrease

The findings in Section 4.3 and Section 4.4 point to a consistent mechanism. The curved shell is initially stiffer than the flat plate, because the term N_θ/R in the radial equilibrium equation of the shell transfers part of the load to the hoop membrane force. The hoop compression measured near the contact in the first millisecond (Fig. 6a) is the sign of this contribution. The contribution exists as long as the shell keeps its local shape. As the dent grows, the hoop stress around the contact turns into tension between 1.4 and 3.6 ms, and the ratio K_{dl}/K_0 falls with curvature from 1.33 to 0.60. The flat plate behaves in the opposite way. In a supported thin plate, membrane tension develops over the span as the deflection exceeds the thickness, and the plate hardens. The hoop tension at the outer arc points of the flat plate reaches 140.7 MPa at the peak force, whereas in the curved panels it stays at 2.5 to 31.1 MPa (Fig. 6c). In the same series the two panel types evolve in opposite directions before damage. The flat plate hardens through span-wide membrane tension, whereas the curved shell softens by losing the hoop compression path. Since the probe points are limited to a single position through the thickness, this evidence does not separate the membrane and bending shares. A full verification of the mechanism requires the through-thickness distribution of the resultant forces.

After damage begins, both types lose stiffness, but the loss of the curved shell is large. The secant stiffness at the peak is 99 per cent of the initial stiffness in the flat plate and 41 to 70 per cent in the curved panels. That the contact duration agrees with the quasi-static expression built with K_{sec} (Fig. 7a) is consistent with the interpretation that the effective spring constant at the peak falls with curvature. This consistency is not a prediction, because K_{sec} is read from the same response. The independent result is that the initial stiffness reads the series in the opposite direction. The contact duration computed with K_0 shortens with curvature and the peak force rises, whereas the measured values change in the opposite direction. The expectation in the literature that the peak force increases as the stiffness increases [19, 28, 29] has been established for a stiffness increase that is retained up to the peak, such as thickness or fibre volume fraction. An increase in thickness raises both K_0 and K_{sec}, whereas in this series curvature raised only K_0. The opposite trend observed in the curved shell therefore does not contradict the expectation in the literature.

The secant stiffness framework also brings the differing reports on which variable the contact duration depends on to the same point. In the analytical solution derived for three-dimensional woven plates it was

reported that the contact duration depends very little on the impactor mass [33]. That result belongs to the wave-controlled or small mass regime. In this series, in which the impactor mass exceeds two hundred times the panel mass, the response is quasi-static according to Olsson's criterion [34] and the measured contact duration is consistent with $\sqrt{(m/K_{sec})}$. The two reports belong to different regimes and cannot be compared without reporting the mass ratio.

5.2. Physical meaning of the cohesive area measure

Equation 12 shows that the cohesive damage variable is a ratio of stiffness loss and that it is related to the dissipated energy through the separation ratio r of the card in a strongly nonlinear way. The value of r comes only from the parameters of the card and is much larger than one in typical cohesive cards, because the penalty stiffness is chosen large enough to suppress separation up to damage initiation. This ratio, which is 112.6 in the card used, means that at a position where the damage variable has reached one half less than one per cent of the fracture energy has been dissipated. With the same card the area of the 0.5 threshold came out 3 to 12 times the energy-equivalent area and the fully separated area 1.6 to 4.5 times below it. The two thresholds rank the same six panels differently. The flat plate and the half cylinder are the most damaged at the 0.5 threshold and at the same level as the other panels at the 0.999 threshold. A curvature trend built with the threshold area depends in this series on the choice of the threshold.

The finding does not mean that the damage variable is wrong. The variable does the job for which it is defined and reduces the interface stiffness correctly. The problem lies in a map of stiffness loss being read as an energy map. The energy-equivalent area corrects this reading with Equation 12. The product $G_c A_E$ equals the fracture energy dissipated at the interface and its result contains no threshold. In terms of experimental comparison the two measures correspond to different things. Ultrasonic scanning shows the region in which the acoustic impedance of the interface changes, in other words the band that is separated or has undergone a marked stiffness loss. This band is wider than the region in which the damage variable reaches 0.999 and narrower than the region in which it is greater than zero. If the numerical delamination area is to be compared with an experimental scan, the threshold must be chosen so as to correspond to this band and the choice must be reported. The energy-equivalent area, on the other hand, is compared not with an experimental area but with the energy dissipated at the interface.

The advantage of A_E is not unlimited. As shown in Section 4.8, A_E computed from the same damage field changes with the value of r of the card and lies between $\Sigma a_i d_i$ and the fully separated area. This card dependence differs qualitatively from the dependence of the threshold areas on the threshold. The threshold is the choice of the analyst, whereas r comes from the measurable strength, stiffness and fracture energy values of the card. In the measurement resolution test the coefficient of variation of A_E is between 1.3 and 17.6 per cent, and that of the fully separated area, except for a5, between 16.3 and 40.5 per cent (Table 9). A_E is clearly more stable than the fully separated area and less stable than the area of the 0.5 threshold. The results show not that A_E is superior under all conditions, but that it is the only area measure related by definition to the dissipated energy.

Equation 12 was derived for a card in which the three modes have equal parameters. In real composite interfaces G_{IIc} is generally markedly larger than G_{Ic}. In surface-based cohesive behaviour in mixed mode, the damage variable is defined in the same form as in Equation 10, but with the effective separation and with initiation and failure separations that depend on the mode mixity. For equal penalty stiffness, the quadratic initiation criterion and the Benzeggagh-Kenane law,

$$\delta_0^m = \delta_0^n \delta_0^s \sqrt{\frac{1+\beta^2}{(\delta_0^s)^2+(\beta\,\delta_0^n)^2}}, \qquad \delta_f^m = \frac{2[G_{Ic}+(G_{IIc}-G_{Ic})B^{\eta_{BK}}]}{K\,\delta_0^m}, \qquad r(B) = \frac{\delta_f^m}{\delta_0^m} \tag{14}$$

is written. Here β is the ratio of the shear separation to the normal separation and $B = \beta^2/(1+\beta^2)$ the ratio of the shear energy to the total energy. When the mode mixity stays constant during loading, the derivation of Equation 10 and Equation 11 is repeated unchanged and Equation 12 remains valid with $r(B)$ substituted for r. The dissipated energy density is in this case multiplied by $G_c(B)$, and the energy-equivalent area is weighted with the $G_c(B)$ value of each position. When the mode mixity changes during loading, the relation remains

approximate because the damage variable depends on the history. For the mode-dependent card used in the T300/5208 study of the first author (t_n^0 = 50 MPa, t_s^0 = 80 MPa, G_{Ic} = 0.26 N/mm, G_{IIc} = 1.002 N/mm, η_{BK} = 1.45, $K = 10^6$ N/mm³) [35], r is 208 in pure mode I and 313 in pure mode II and stays between 207 and 327 with the mode mixity (Fig. 14a). In this range 0.3 to 0.5 per cent of the fracture energy is dissipated at a position with d = 0.5 and 75 to 83 per cent at d = 0.999. When the penalty stiffness is lowered to 10^5 N/mm³, r falls to between 21 and 33 and the share at d = 0.5 becomes 3.0 to 4.6 per cent. In mode-dependent and softer cards too, the area of the 0.5 threshold represents a small fraction of the dissipated energy, and the result of Section 4.6 does not change in direction. The assessment belongs to the relation itself. Since the damage field of a model solved with a mode-dependent card is not available in this study, the numerical values of the ratios between the threshold areas and A_E for that card must be computed separately.

5.3. Comparison with previous studies

In the curvature screening of the first author on unidirectional T300/5208 laminates, the peak force of the intralaminar-only damage model reached its maximum at intermediate curvature and fell on both sides [35]. In this series, by contrast, the peak force is largest in the flat plate, falls at the first curvature level and stays in a narrow band within the curved family. The difference between the two series lies in the laminate thickness and the stacking. The panels there are 5 mm thick, have nine interfaces and are loaded with 33.5 J, those here are 1 mm, with three interfaces and 6.70 J. In the thick laminate the maximum deflection stays of the order of the thickness at 5.2 mm [35] and the membrane effects are limited. In the thin woven shell, by contrast, the deflection reaches eight to ten times the thickness, the flat plate hardens and the curved shell softens. From the peak force and maximum displacement reported in that study [35], K_{sec} and χ can be computed for the model with cohesive interfaces. At an impact energy of 33.5 J and a mass ratio between 48 and 76, K_{sec} rises to its highest value of 3524 N/mm at a2 and then falls to 2201 N/mm in the half cylinder, while χ falls with curvature from 0.990 to 0.786. Despite the different material, thickness, energy and mass ratio, the fall of χ is in the same direction as the fall from 0.907 to 0.748 here. Since the initial stiffness and the contact duration were not reported in that series, the independent test made with K_0 could not be repeated there.

The finding of Belingardi and Vadori that both the first damage force and the peak force rise linearly with the number of plies [19] corresponds, in the framework of this study, to K_0 and K_{sec} rising together with thickness. The simultaneous increase of the contact duration and the peak force in repeated impact [29] has been explained by the change of the local stiffness between impacts and cannot be compared directly with this single-impact series. The doubly curved panel study of Zhao and co-workers [30] scanned the other variables while holding the curvature ratio constant and therefore provides no comparison data for the effect of curvature itself. No experimental series that scans curvature at constant projected span and reports the secant stiffness exists in the literature. The interpretation of this study is testable. In a thin curved shell struck with the same impactor mass and energy, the ratio K_{dl}/K_0 is expected to fall with curvature and the measured contact duration to remain consistent with $\pi\sqrt{(m/K_{sec})}$.

5.4. Scope and limits

The results belong to a single numerical framework with no experimental counterpart for these six panels. The material card was taken from measured values [38], the formulation has been compared with experiment in woven laminates and in semi-cylindrical woven shells [18, 24, 25], and the global quantities have been shown to be insensitive to the cohesive card [18]. The literature basis supports the formulation, but it does not validate the predicted damage development of the curvature series. The results are therefore presented as numerical relations.

Mesh convergence was not performed. In previous studies with the same formulation the peak force and the displacement converged within a few per cent, whereas the fully separated area deviated by 21 per cent on the coarse mesh [35, 37]. The measurement resolution test showed that at 2.5 mm spacing the fully separated area carries an uncertainty of up to 41 per cent and A_E an uncertainty of up to 18 per cent (Table 9). Comparisons

between panels were therefore made only for differences exceeding this band. That A_E is independent of the mesh has not been shown in this study.

Between the solver total energy balance and the sum of the three physical components there is a residual that grows with curvature from 6.6 to 38.1 per cent. The sum of the physical components matches the applied energy within 0.9 per cent throughout the event, the residual stays below 0.4 per cent of the applied energy up to first damage and shows no relation with the damage measures (Section 4.2). The initial and first damage stiffnesses are therefore independent of the residual. The peak quantities were measured when 15 to 59 per cent of the residual had accumulated. Although it has been shown that the residual is not drawn from the physical components, its source could not be identified, and its growth with curvature is a subject to be investigated in the interaction between cohesive contact and the continuum shell element in curved shells.

The laminate was divided into four sublaminates and only three interfaces were modelled as cohesive. Separation between the plies within a sublaminate is not represented. The energy of a separation that could in reality develop at the interfaces within a sublaminate is collected in the model either at one of the three interfaces or in the intralaminar damage variables. The reported total A_E and the energy dissipated at the interface are therefore not equal to the values that a ply-by-ply modelled laminate would give, and the direction of the deviation cannot be determined from the data of this study. The through-thickness distribution (Fig. 12b) is sampled with three planes spaced 0.25 mm apart. Equation 12 and the definition of A_E, on the other hand, hold separately for each interface. The relation between the threshold areas and A_E depends on the value of r of the card and on the distribution of the damage variable, not on the number of interfaces.

The secant stiffness framework was examined at a single impactor mass and a single energy. Its validity has not been tested in cases where the mass ratio falls close to Olsson's criterion or where the energy increases the share dissipated up to the peak. The peak force in panel a4 was read on an early spike and the peak time of this panel differs from the others, but its secant stiffness at the peak and its contact duration are consistent with the series.

6. Conclusions

The low-velocity impact response of woven T300/914 cylindrical shell panels was examined numerically at six curvature levels at a constant projected span and a constant thickness, with intralaminar and interlaminar damage modelled together.

Curvature raised the initial tangent stiffness by 74 per cent while it lowered the peak impact force by 17.5 to 23.3 per cent and extended the contact duration by 16 to 27 per cent. The mass spring expressions built with the initial stiffness predict these trends in the opposite direction. The divergence begins before damage. The ratio of the secant stiffness at first damage to the initial stiffness is 1.33 in the flat plate and 0.60 in the half cylinder. The secant stiffness at the peak falls by 24 to 29 per cent with curvature, and the measured contact duration is consistent with the quasi-static expression built with this stiffness within 8.9 per cent. Since the secant stiffness is read from the response, this consistency does not show a predictive capability.

The hoop stresses taken along the arc are consistent with the interpretation that the flat plate hardens through membrane tension over the span and that the curved shell loses the hoop compression path around the contact near first damage. At the peak force the mean hoop stress on the outer arc is 140.7 MPa in the flat plate and between 2.5 and 31.1 MPa in the curved panels. The observation rests on a single point through the thickness and does not separate the membrane and bending shares.

The closed-form relation between the damage variable and the dissipated energy was derived from the bilinear cohesive law as $D/G_c = d/(r - (r - 1)d)$, $r = 2G_cK/(t^0)^2$, and extended with $r(B)$ to mode-dependent cards when the mode mixity stays constant. For the card used, with r = 112.6, 0.9 per cent of the fracture energy is dissipated at the 0.5 level of the damage variable. In a mode-dependent card this share is below 0.5 per cent for $K = 10^6$ N/mm³ and below 4.6 per cent for $K = 10^5$ N/mm³. The energy-equivalent area is between 122 and 262 mm². The area of the 0.5 threshold is 3 to 12 times this, the fully separated area 1.6 to 4.5 times below it, and the two thresholds produce opposite rankings for the same panels. The energy-equivalent area contains no threshold, depends on the value of r of the card and is clearly less sensitive to the measurement resolution than the fully separated area.

In the six panels interface separation began while the force was below one third of its peak value and was seen 1 to 2 ms before the first significant drop in the force history. The damage load read from the force drop and the load at which interface separation begins are not the same quantity.

The validity of the secant stiffness framework at different impact energies, impactor masses and damage levels, the mesh independence of the energy-equivalent area and its behaviour in models solved with mode-dependent cards are hypotheses not tested in this study. The results belong to a numerical framework without an experimental counterpart, solved with a single mesh, a single energy and a single impactor mass, and carrying a residual of unidentified source in the energy balance.

Author contribution statement

Onur Gök carried out the conceptualisation, methodology, software, formal analysis, investigation, writing and visualisation. The contribution roles of H. Hüseyin Taşer and Lokman Gemi.

Acknowledgements

This research did not receive any specific grant from funding agencies in the public, commercial, or not-for-profit sectors.

Declarations

Conflict of interest. The authors declare no known conflict of interest related to this work.

Data availability. The data supporting the findings of this study are given in the figures and tables of the article.

Declaration of the use of an artificial intelligence assisted tool. During the preparation of this work an artificial intelligence assisted language tool was used solely for the translation of the text from Turkish into English. The tool was not used in producing the scientific content or in obtaining, analysing or interpreting the data. The authors reviewed and edited the content and take full responsibility for the content of the published article.

References

[1] Symons, D. D. (2000). Characterisation of indentation damage in 0/90 lay-up T300/914 CFRP. Composites Science and Technology, 60, 391–401.

[2] Symons, D. D., & Davis, G. (2000). Fatigue testing of impact-damaged T300/914 carbon-fibre-reinforced plastic. Composites Science and Technology, 60, 379–389.

[3] Hallett, S. R. (2000). Three-point beam impact tests on T300/914 carbon-fibre composites. Composites Science and Technology, 60, 115–124.

[4] Tita, V., de Carvalho, J., & Vandepitte, D. (2008). Failure analysis of low velocity impact on thin composite laminates: experimental and numerical approaches. Composite Structures, 83, 413–428.

[5] Feng, D., & Aymerich, F. (2014). Finite element modelling of damage induced by low-velocity impact on composite laminates. Composite Structures, 108, 161–171.

[6] Shi, Y., Swait, T., & Soutis, C. (2012). Modelling damage evolution in composite laminates subjected to low velocity impact. Composite Structures, 94, 2902–2913.

[7] Lou, X., Cai, H., Yu, P., Jiao, F., & Han, X. (2017). Failure analysis of composite laminate under low-velocity impact based on micromechanics of failure. Composite Structures, 163, 238–247.

[8] Huang, L., Tao, Y., Sun, J., Zhang, D., & Zhao, J. (2023). Assessment of numerical modeling approaches for thin composite laminates under low-velocity impact. Thin-Walled Structures, 191, 111053. https://doi.org/10.1016/j.tws.2023.111053
[9] Giasin, K., Dhakal, H. N., Featherson, C. A., Pimenov, D. Y., Lupton, C., Jiang, C., et al. (2022). Effect of fibre orientation on impact damage resistance of S2/FM94 glass fibre composites for aerospace applications: an experimental evaluation and numerical validation. Polymers, 14, 95.
[10] Han, L., Qi, H., Yang, J., Chu, F., Lin, C., Liu, P., & Zhang, Q. (2024). Study on the low-velocity impact response and damage mechanisms of thermoplastic composites. Polymers, 16, 791.
[11] Huang, Y., EShun, F. T., Hu, J., Zhang, X., Zhao, J., Zhang, S., et al. (2023). Research on low-velocity impact response of novel short-fiber-reinforced composite laminates. Polymers, 15, 840.
[12] Mohsin, M. A. A., Iannucci, L., & Greenhalgh, E. S. (2021). Experimental and numerical analysis of low-velocity impact of carbon fibre-based non-crimp fabric reinforced thermoplastic composites. Polymers, 13, 3642.
[13] Vlach, J., Doubrava, R., Ruzek, R., Raska, J., Hornas, J., & Kadlec, M. (2022). Strain-field modifications in the surroundings of impact damage of carbon/epoxy laminate. Polymers, 14, 3243.
[14] Guo, S., Li, X., Liu, T., Bu, G., & Bai, J. (2022). Parametric study on low-velocity impact (LVI) damage and compression after impact (CAI) strength of composite laminates. Polymers, 14, 5200.
[15] Liu, B., Wang, F., Zheng, Y., Huang, J., Jiang, S., & Zhang, W. (2026). Effect of thickness and stitch density on low-velocity impact and compression after impact properties of stitched composite laminates. Polymers, 18, 791.
[16] Liu, B., Lai, J., Liu, H., Huang, Z., Liu, T., Xia, Y., & Zhang, W. (2023). Finite element analysis of the effect for different thicknesses and stitching densities under the low-velocity impact of stitched composite laminates. Polymers, 15, 4628.
[17] Liu, B., Lai, J., Liu, H., Huang, Z., Liu, B., Peng, Z., & Zhang, W. (2023). Experimental and numerical analysis of stitched composite laminates subjected to low-velocity edge-on impact and compression after edge-on impact. Polymers, 15, 2484.
[18] Ferreira, L. M., Coelho, C. A. C. P., & Reis, P. N. B. (2023). Effect of cohesive properties on low-velocity impact simulations of woven composite shells. Applied Sciences, 13, 6948. https://doi.org/10.3390/app13126948
[19] Belingardi, G., & Vadori, R. (2003). Influence of the laminate thickness in low velocity impact behavior of composite material plate. Composite Structures, 61, 27–38.
[20] Ge, X., Zhang, P., Zhao, F., Liu, M., Liu, J., & Cheng, Y. (2022). Experimental and numerical investigations on the dynamic response of woven carbon fiber reinforced thick composite laminates under low-velocity impact. Composite Structures, 279, 114792.
[21] Olhan, S., Antil, B., & Behera, B. K. (2025). Low-velocity impact and quasi-static post-impact compression analysis of woven structural composites for automotive: influence of fibre types and architectural structures. Composite Structures, 352, 118676.
[22] Wu, Z., Wu, C., Liu, Y., Cheng, X., & Hu, X. (2020). Experimental study on the low-velocity impact response of braided composite panel: effect of stacking sequence. Composite Structures, 252, 112691.
[23] Hongkarnjanakul, N., Bouvet, C., & Rivallant, S. (2013). Validation of low velocity impact modelling on different stacking sequences of CFRP laminates and influence of fibre failure. Composite Structures, 106, 549–559.
[24] Yang, B., Chen, Y., Lee, J., Fu, K., & Li, Y. (2021). In-plane compression response of woven CFRP composite after low-velocity impact: modelling and experiment. Thin-Walled Structures, 158, 107186.
[25] Kumar, Y., Rezasefat, M., Amico, S. C., Manes, A., Dolez, P. I., & Hogan, J. D. (2024). Comparison of two progressive damage models for predicting low-velocity impact behavior of woven composites. Thin-Walled Structures, 197, 111611.
[26] Zhang, Y., Feng, J., Yan, J., Guo, Q., Sun, Z., Zhang, D., et al. (2025). Effect of weave pattern on the low-velocity impact properties of 3D woven composites. Thin-Walled Structures, 209, 112969.
[27] Jing, K., Zhou, H., Wang, H., Yan, H., & Xie, S. (2024). Multiscale damage and low-velocity impact study of three-dimensional woven composites. Thin-Walled Structures, 202, 112132.

[28] Kazemianfar, B., & Nami, M. R. (2021). Influence of oblique low velocity impact on damage behavior of 2D and 3D woven composites: experimental and numerical methods. Thin-Walled Structures, 167, 108253.
[29] Rezasefat, M., Gonzalez-Jimenez, A., Giglio, M., & Manes, A. (2021). Numerical study on the dynamic progressive failure due to low-velocity repeated impacts in thin CFRP laminated composite plates. Thin-Walled Structures, 167, 108220.
[30] Zhao, H., Li, C., Fu, Y., Oyarhossein, M. A., Habibi, M., & Safarpour, H. (2023). Quasi-static indentation, low-velocity impact, and resonance responses of the laminated double-curved panel considering various boundary conditions. Thin-Walled Structures, 183, 110360.
[31] Gemi, L., Azeem, M., Yazman, Ş., Kayrıcı, M., & Gök, O. (2024). Investigation of mechanical properties and damage development of filament wound GFRP composite pipes by ring tensile test. Necmettin Erbakan University Journal of Science and Engineering, 6, 93–104. https://doi.org/10.47112/neufmbd.2024.34
[32] Güven, Z. K., Madenci, E., Gök, O., & Gemi, L. (2026). Low velocity impact behaviour of filament-wound GFRP tubes: combined effects of winding angle and layer number supported by a Hashin-based cohesive finite element model. Composite Structures, 397, 120869. https://doi.org/10.1016/j.compstruct.2026.120869
[33] Zhang, Y., Wei, H., Gong, Z., & Zhang, C. (2025). Analytical solution for low-velocity impact response of three-dimensional woven composite plates considering three-dimensional heterogeneity. Thin-Walled Structures, 215, 113588.
[34] Olsson, R. (2000). Mass criterion for wave controlled impact response of composite plates. Composites Part A: Applied Science and Manufacturing, 31, 879–887. https://doi.org/10.1016/S1359-835X(00)00020-8
[35] Gök, O. (2026). Effect of curvature height on the low-velocity impact behaviour of unidirectional T300/5208 CFRP laminated shell panels: a comparative numerical parametric analysis of intralaminar + interlaminar and intralaminar-only models. Polymers, 18, 1290. https://doi.org/10.3390/polym18111290
[36] Gök, O. (2026). Effect of stacking sequence on the low-velocity impact behaviour of T300/5208 carbon/epoxy laminates: an intralaminar Hashin-CDM based numerical study. Black Sea Journal of Engineering and Science, 9, 2094–2107. https://doi.org/10.34248/bsengineering.1962591
[37] Gök, O. (2026). Effect of stacking architecture on the low-velocity impact behaviour of carbon fibre reinforced polymer plates: a physics-informed screening framework based on lamination parameters, orientation entropy and an interface mismatch relation. Polymer, 363, 130590. https://doi.org/10.1016/j.polymer.2026.130590
[38] Hou, J. P., & Ruiz, C. (2000). Measurement of the properties of woven CFRP T300/914 at different strain rates. Composites Science and Technology, 60, 2829–2834.